Available online at www.sciencedirect.com
ScienceDirect
Comput. Methods Appl. Mech. Engrg. 383 (2021) 113910
Computer methods in applied mechanics and engineering
www.elsevier.com/locate/cma

A mixed interface-capturing/interface-tracking formulation for thermal multi-phase flows with emphasis on metal additive manufacturing processes

Qiming Zhu, Jinhui Yan*

Department of Civil and Environmental Engineering, University of Illinois at Urbana–Champaign, United States of America

Received 17 February 2021; received in revised form 22 April 2021; accepted 4 May 2021
Available online 18 May 2021

Abstract

High fidelity thermal multi-phase flow simulations are in much demand to reveal the multi-scale and multi-physics phenomena in metal additive manufacturing (AM) processes, yet accurate and robust predictions remain challenging. In this paper, we present a novel computational framework by mixing interface-capturing/interface-tracking methods for simulating the thermal multi-phase flows in metal AM applications, focusing on better handling the gas-metal interface, where AM physics, such as phase transitions and laser-material interactions, mainly takes place. The framework, built on level set method and variational multi-scale formulation (VMS), features three major contributions: (1) a simple computational geometry-based re-initialization approach, which maintains excellent signed distance property on unstructured meshes, re-constructs an explicit representation of gas-metal interface from the level set, and facilitates the treatment of the multiple laser reflections during keyhole evolution in AM processes; (2) a fully coupled VMS formulation for thermal multi-phase governing equations, including Navier-Stokes, level set convection, and thermodynamics with melting, solidification, evaporation, and interfacial force models; and (3) a three-level recursive preconditioning technique to enhance the robustness of linear solvers. We first compare the geometry-based re-initialization with the Eikonal partial differential equation (PDE)-based approach on two benchmark problems on level set convection and bubble dynamics. The comparison shows the geometry-based approach attains equivalent and even better performance on key criteria than the PDE-based counterpart. We then apply the developed framework to simulate two AM experiments, which Argonne National Laboratory has recently conducted using in-situ high-speed, high-energy x-ray imaging. The proposed framework's accuracy is assessed by thoroughly comparing the simulated results against experimental measurements on various quantities. We also report important quantities that experiments cannot measure to show the modeling capability.

Keywords: Geometry based re-initialization; VMS; Level set method; Additive manufacturing

1. Introduction

Multi-phase flows ubiquitously exist in natural and engineering systems. Their numerical simulations have advanced many scientific and technological areas, such as bubble dynamics, propeller design, oil refining, and

* Corresponding author.
E-mail address: yjh@illinois.edu (J. Yan).

https://doi.org/10.1016/j.cma.2021.113910

chemical reaction optimization, to name a few. In recent years, multi-phase flow simulations are attracting attention from metal additive manufacturing (AM): a type of technology with the potential to reshape various industries because of its superior capability to print complex metallic parts directly from digital models without the constraints of traditional manufacturing technologies [1]. In metal AM simulations, thermal multi-phase flow-based models, which solve coupled multi-phase Navier–Stokes and thermodynamics equations with phase transitions, are widely deemed the state-of-the-art predictive tools with the highest fidelity. They complement the expensive experiments, such as in-situ high-speed, high-energy x-ray imaging, to reveal the multi-scale and multi-physical phenomena and derive the process–structure–property–performance relationship in metal AM. For the past several years, many researchers have proposed various methods in this direction. For example, Lawrence Livermore National Laboratory developed a thermal-fluid solver using the Arbitrary-Lagrangian Eulerian (ALE) technique [2–5]; Yan's group at National University of Singapore developed a set of volume-of-fluid (VOF) based thermal-fluid models to simulate metal AM problems, including directed energy deposition (DED) and multi-layer and multi-track laser powder bed fusion (LPBF) processes [6–10]; Panwisawas et al. also used a VoF approach by using OpenFOAM to analyze the inter-layer and inter-track void formation [11]; Lin et al. developed a control-volume finite element approach to simulate DED and LPBF processes [12,13]. Li et al. developed a thermal-fluid model by combining the level set method and Lagrangian particle tracking to investigate powder–gas interaction in LPBF processes [14]. One should note that the above is not a complete literature review of recent method developments. A literature review is also not this paper's focus. For a comprehensive survey on metal AM modeling, we refer interested readers to a recent review article in [15].

Despite the progress that has been made, thermal multi-phase flow simulations for metal AM applications still impose tremendous challenges on numerical methods. The first challenge is how to treat the gas-metal interface, where AM physics, such as phase transitions and laser-material interactions, mainly occurs. There are two types of approaches to handle material interface evolution in multi-phase flows. This first option is interface-tracking, including Arbitrary-Lagrangian Eulerian (ALE) [16], front-tracking [17], boundary-integral [18], and space–time [19]. The material interface evolution in interface-tracking approaches is explicitly represented by a deforming and compatible mesh that moves with the material interface. These approaches possess high accuracy per degree of freedom and have been applied to many free-surface flow problems [20]. However, mesh motion and even re-meshing are often required if the material interface undergoes large deformations or singular topological changes, which turn out to be very common in metal AM applications even without considering powders. Another option is interface-capturing, including level set [21,22], front-capturing [23], volume-of-fluid (VOF) [24], phase field [25–31], and diffuse-interface methods [32,33]. In interface-capturing approaches, an auxiliary field is defined in an Eulerian domain to represent the interface implicitly. The evolution of the interface is governed by an additional scalar partial differential equation (PDE). Because the interface evolution is embedded in the PDE, these approaches can automatically handle topological interface changes without requiring mesh motion or re-meshing procedures. Interface-capturing approaches have been widely applied to a wide range of interfacial problems, including bubble dynamics [34–36], jet atomization [37], and free-surface flows [38,39]. However, interface-capturing approaches need higher mesh resolution around the interface to compensate for their lower accuracy. Furthermore, in metal AM applications, an implicit representation of the gas-metal interface imposes technical burdens to handle the laser-material interaction, such as the multiple laser reflections on the melt pool interface.

The second challenge is that metal AM processes, compared with other multi-phase flow problems, involve more physics interplay at a wide range of spatiotemporal scales, including thermodynamics, multi-phase melt pool fluid dynamics, phase transitions (e.g., melting, solidification, evaporation, and condensation), laser–metal interaction, and interface topological changes. Besides, the property ratios are larger than those of two-phase flows in other engineering problems (e.g., free-surface flows in ocean engineering). The resulting linear systems have higher condition numbers due to these aspects, introducing convergence issues for partitioned methods and necessitating more robust coupling solution strategies.

Aiming to address the two challenges, we develop a mixed interface-capture/interface-tracking formulation for thermal multi-phase flows for metal AM applications. The reason we call it a mixed formulation is two-fold. (1) We first utilize a level set method to model the gas-metal interface evolution (interface capturing). (2) The gas-metal interface is then explicitly re-constructed by triangulating the intersection points between the zero level set and mesh element edges (interface tracking). Such combination takes full advantages of the level set method's capability of handling topological interface changes and the convenience of an explicit gas–metal interface representation

on treating multiple laser reflections. To ensure the level set field's signed distance property, we abandon the Eikonal equation (PDE-based) re-initialization used in our previous work and develop a purely computational geometry-based approach in this paper. We show that the geometry-based re-initialization approach attains equivalent and sometimes even better performance than the PDE-based counterpart. The method is very efficient, simple to implement on unstructured tetrahedral meshes, and simultaneously constructs a triangulation with an octree data structure for explicitly representing the interface, facilitating the ray-tracing process for multiple laser reflections.

The variational multiscale formulation (VMS) is utilized as a turbulence model to solve the coupled multi-phase Navier–Stokes, level set, and thermodynamics equations augmented with melting, solidification, and evaporation models. Although the characteristic length scales of metal AM processes are small, the melt pool flow speed can reach to order of m/s, resulting in non-negligible turbulence. Research in [40] showed the effects of with and without turbulence model on the predictions of melt pool dimensions. VMS, because of its variational consistency, flexibility, and previous success in multi-phase flow simulations, is a very natural choice for the problems considered in this paper. We employ density-scaled continuous surface force (CSF) models to handle surface tension, Marangoni stress, recoil pressure, laser flux, and other boundary conditions on the gas-metal interface. The generalized-α method is utilized to integrate the VMS formulation over time. We employ Newton's method to linearize the nonlinear nodal systems at each time step, which leads to a two-stage predictor/multi-corrector algorithm. The resulting linear system is solved in a fully coupled fashion to enhance robustness by using a generalized minimal residual method (GMRES) with a three-level recursive preconditioning technique we proposed.

This paper is structured as follows. Section 2 presents the details of the computational framework, including geometry-based re-initialization, governing equations, ray-tracing for laser reflections, VMS formulation, time-integration, linear solver, preconditioning, and mass-fixing. Section 3 presents four numerical examples to test the performance of the proposed framework. The first two problems are used to compare the performance between the geometry-based re-initialization and the PDE-based re-initialization. The next two are the real-world problems, aiming to assess the proposed framework's accuracy and predictive capability for metal AM applications. The simulation results are carefully compared with experimental data from Argonne National Laboratory. The quantities that experiments cannot measure are also reported. We summarize the contributions and limitations of this paper and specify future directions in Section 4.

2. Computational methods

2.1. Level set method

Let Ω denote the domain of a metal AM problem, consisting of the metal subdomain Ω_m and gas subdomain Ω_g, and the gas–metal interface Γ_I is implicitly represented as

$$\Gamma_I = \{\boldsymbol{x} | \phi(t, \boldsymbol{x}) = 0, \forall \boldsymbol{x} \in \Omega\} \tag{1}$$

where $\phi(t, \boldsymbol{x})$ is a level set field, whose value is the signed distance function from $\boldsymbol{x}$ to the gas-metal interface Γ_I, namely,

$$\phi(t, \boldsymbol{x}) = \begin{cases} dist(\boldsymbol{x}, \Gamma_I) & \text{if } \boldsymbol{x} \in \Omega_m \\ -dist(\boldsymbol{x}, \Gamma_I) & \text{if } \boldsymbol{x} \in \Omega_g \end{cases} \tag{2}$$

The evolution of ϕ is governed by the following convection equation

$$\frac{\partial \phi}{\partial t} + \boldsymbol{u} \cdot \nabla \phi = 0 \tag{3}$$

where $\boldsymbol{u}$ is the fluid velocity.

2.1.1. PDE-based re-initialization

The signed distance property of level set functions can be polluted by strong convective velocity. One popular re-initialization (or re-distancing) technique is to solve the following pseudo-time dependent Eikonal equation with the constraint on the gas-metal interface.

$$\frac{\partial \phi_d}{\partial \tilde{t}} + \text{sign}(\phi)(\|\nabla \phi_d\| - 1) = 0 \qquad \text{in } \Omega_m \text{ and } \Omega_g \tag{4}$$

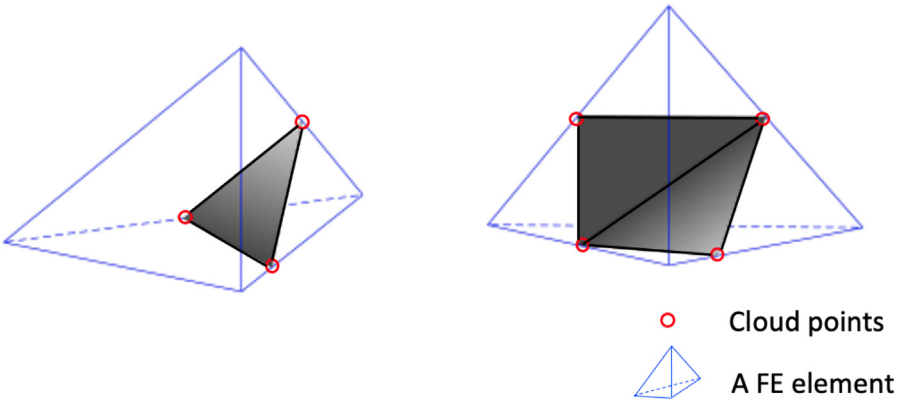

Fig. 1. Element-wise triangulation. First intersection scenario: Three cloud points and one triangle (left). Second intersection scenario: Four cloud points and two triangles (right).

$$\phi_d = 0 \qquad \text{on } \Gamma_I \tag{5}$$

$$\phi_d(\tilde{t} = 0, \boldsymbol{x}) = \phi(t, \boldsymbol{x}) \qquad \text{in } \Omega_m \text{ and } \Omega_g \tag{6}$$

where ϕ_d is the re-initialized level set, $\tilde{t}$ is the pseudo-time. The pseudo-temporal discretization ($\Delta\tilde{t}$) is scaled by the element length around the interface. The technique was employed in our previous work in conjunction with the variational multi-scale method (VMS) for many multi-phase problems [41–44]. The major advantage of this approach is that it only needs to solve a PDE without requiring one particular mesh type. However, an effective pseudo-time integration scheme is necessary, and a linear solver is needed if implemented implicitly. How to choose the pseudo-time step can be tricky for unstructured meshes, and the choice has a significant effect on the accuracy. Besides, lacking an explicit representation of the gas-metal interface still imposes technical burdens on handling the multiple laser reflections in metal AM problems.

2.1.2. Geometry-based re-initialization

In this paper, we propose a computational geometry-based re-initialization approach specifically designed for metal AM simulations using unstructured meshes. The concept of using geometry for re-initializing level set field can date back to [45,46] but has not been employed in thermal multi-phase flows. As we show below, the approach is simple to implement on unstructured tetrahedral meshes and re-constructs an explicit interface representation from the level set field, which provides significant convenience to handle the multiple laser reflections in metal AM processes.

The first step of the geometry-based re-initialization is to extract all the intersection points between the gas–metal interface ($\phi = 0$) and every element edge of the mesh. To differentiate from the intersections between laser rays and gas-metal interface, we call these intersections "cloud points", denoted as a set by Ξ. The cloud points' locations are obtained by the following procedure. We first check the signs of level-set function value on the nodes of each element. If the signs change, this element intersects with the gas–metal interface. Considering that iso-parametric elements are employed, we can get the parametric coordinates $\boldsymbol{\xi}$ by solving $\sum N_A(\boldsymbol{\xi})\phi_A = 0$, where $N_A(\boldsymbol{\xi})$ and ϕ_A are the basis function and nodal level set value. We then use parametric coordinates $\boldsymbol{\xi}$ to get the physical coordinates of the cloud points by $\sum N_A(\boldsymbol{\xi})\boldsymbol{x}_A$, where $\boldsymbol{x}_A$ is the nodal physical coordinates. The linear tetrahedron element is used in our paper. After all the cloud points' coordinates are identified, a triangulation of the cloud points is constructed. At first glance, the triangulation process seems to require sophisticated algorithms, such as Delaunay triangulation [47]. The triangulation can be performed in an element-wise fashion and is suitable for parallel computing. Fig. 1 shows the only possible two intersection scenarios between a tetrahedral element and the gas–metal interface. In the first scenario, the intersection results in three cloud points, and a triangle can be formed by connecting each two of them. In the second scenario, the intersection results in four cloud points, and two triangles can be formed similarly. Then all the triangles are catenated to construct a triangulation that forms an explicit representation of the gas–metal interface.

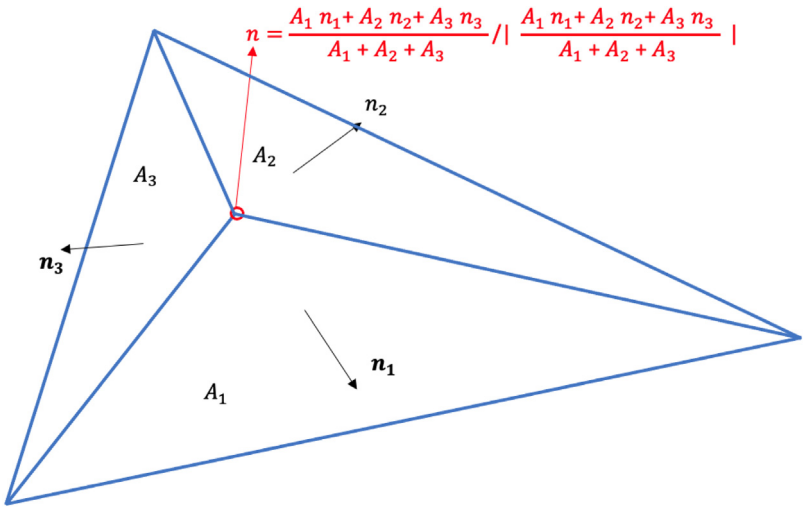

Fig. 2. Unit normal vector definition of a cloud point in the triangulation.

The second step is to calculate the unit normal vector of the cloud points based on their triangulation. Because the triangulation is only C_0 continuous on the cloud points, the normal vector, as shown in Fig. 2, is computed by averaging of the unit normal vector of the triangles (weighted by their areas) associated with this cloud point, namely,

$$\boldsymbol{n} = \frac{\sum_i \boldsymbol{n}_i A_i}{\sum_i A_i} \Big/ \left| \frac{\sum_i \boldsymbol{n}_i A_i}{\sum_i A_i} \right| \tag{7}$$

where A_i and $\boldsymbol{n}_i$ are the area and unit normal vector of the triangles.

The third step is to restore signed distance for each mesh node by minimizing its normal distance to the gas–metal interface represented by the triangulation of the cloud points. For a mesh node denoted by $\boldsymbol{x}_i$, the re-initialized level set $\phi_d(t, \boldsymbol{x}_i)$ is defined as

$$\phi_d(t, \boldsymbol{x}_i) = \text{sign}[\phi(\boldsymbol{x}_i)] |(\boldsymbol{x}_i - \boldsymbol{y}_m) \cdot \boldsymbol{n}_m| \tag{8}$$

where $\boldsymbol{n}_m$, defined by Eq. (7), is the unit normal vector of the cloud point $\boldsymbol{y}_m$, which has the minimal Euclidean distance to $\boldsymbol{x}_i$, namely,

$$m = \arg\min_{j \in \Xi} \left(|\boldsymbol{x}_i - \boldsymbol{y}_j| \right) \tag{9}$$

One can find the minimal distance and the corresponding cloud point by looping all cloud points. The complexity of this brute force approach for each mesh node is $O(N)$ if there are N cloud points. The approach can be intractable in metal AM problems, given the large mesh size that also results in a large number of cloud points. To speed up the minimization, we first organize the cloud points Ξ into an octree structure based on the bounding boxes of the domain. Fig. 3(a) and (b) show a 2D presentation of the octree construction process. The minimal distance between a mesh node $\boldsymbol{x}_i$ and the cloud points is identified by a traversal on the octree with pruning. The algorithm is described as follows.

- **Step 3.1:** Randomly pick a cloud point from the octree, and set the distance between $\boldsymbol{x}_i$ and this cloud point to r_m and set the cloud point's index to m. Then, start the traversal from the octree root.
- **Step 3.2:** For each tree node, calculate the minimum distance between $\boldsymbol{x}_i$ and the associated bounding box if $\boldsymbol{x}_i$ is outside the current bounding box. If the distance is bigger than r_m, skip this path. If not, go to **step 3.3**.
- **Step 3.3:** Repeat the process described in **step 3.2** for the 8 sub-bounding boxes. If arriving at a leaf of the octree, calculate the distance between $\boldsymbol{x}_i$ and the cloud point associated with this leaf. Set this distance to r_m and the cloud point's index to m, if the distance is smaller than r_m.
- **Step 3.4:** Return m and r_m, and calculate re-initialized $\phi_d(t, \boldsymbol{x}_i)$ based on Eq. (8).

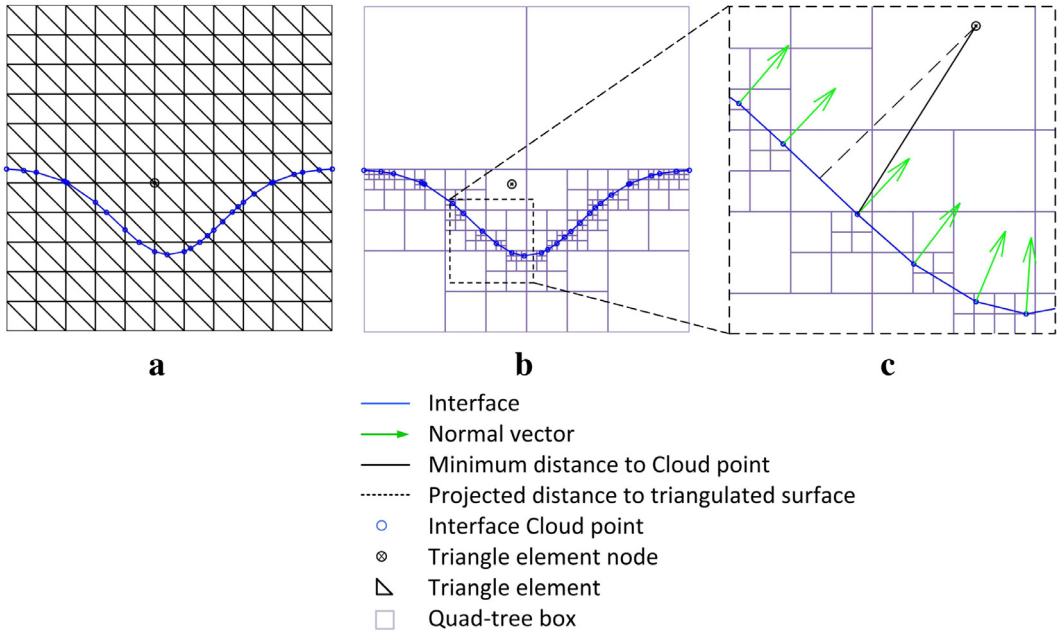

Fig. 3. A 2D description of the geometry-based re-initialization. (a): Cloud points. (b): Quad-tree structure of the cloud points. (c) Computation of signed distance function.

It is easy to show that the complexity of this approach for each mesh node is only $O(logN)$. Compared with the PDE-based approach, this geometry-based approach is more efficient and simple to implement. Firstly, the PDE-based approach involves many user-defined numerical parameters (e.g., interface thickness and pseudo time step), the choices of which influence the efficiency. Secondly, how long one integrates the Eikonal equation over pseudo time, the employed time-integration scheme, linear solver/preconditioner (if an explicit scheme is utilized) also affect the efficiency of the PDE-based approach. In contrast, the geometry-based counterpart recovers signed-distance property everywhere and does not involve any of these user-defined parameters. Our non-exhaustive experience shows the geometry-based approach is slightly faster than the PDE-based approach we developed in [41–44]. More importantly, during the re-initialization, an explicit gas-metal interface, described by the triangulation of cloud points, is constructed, which provides tremendous convenience in the heat laser model, as we will show later.

2.2. Governing equations of thermal multi-phase flows

2.2.1. Property evaluation

The thermal multi-phase flows are governed by a unified mathematical model, in which the material properties are phase-dependent. In the model, the level set field is utilized to distinguish the gas phase and the metal phase, and the liquid fraction f_l is utilized to distinguish the liquid phase and the solid phase in the metal. For a material property $\chi(\phi, f_l)$ (e.g., density, dynamic viscosity, specific heat, and thermal conductivity), it is evaluated by the following linear combination

$$\chi(\phi, f_l) = H(\phi)\left[(1 - f_l)\chi_s + f_l\chi_l\right] + \left[1 - H(\phi)\right]\chi_g \tag{10}$$

where χ_s, χ_l, and χ_g are the values of the material property in the solid, liquid, and gas phases, respectively. $H(\phi)$ is a regularized Heaviside function, defined as

$$H(\phi) = \begin{cases} 0 & \phi \leq -\epsilon \\ \frac{1}{2}\left(1 + \frac{\phi}{\epsilon} + \frac{1}{\pi}sin(\frac{\phi\pi}{\epsilon})\right) & |\phi| < \epsilon \\ 1 & \phi \geq +\epsilon \end{cases} \tag{11}$$

where ϵ is a numerical gas–metal interface thickness, scaling with the local element size. f_l is a function of temperature T, defined as

$$f_l = \begin{cases} 0 & T < T_s \\ \frac{T-T_s}{T_l-T_s} & T_s \leq T \leq T_l \\ 1 & T > T_l \end{cases} \tag{12}$$

where T_s and T_l are the solidus and the liquidus temperature of the metal material, respectively.

2.2.2. Navier–Stokes equations of multi-phase flows

The fluid motion obeys the following Navier–Stokes equations.

$$\rho\left[\frac{\partial \boldsymbol{u}}{\partial t} + \nabla\cdot(\boldsymbol{u}\otimes\boldsymbol{u}) - \boldsymbol{g}\right] - \nabla\cdot(-p\boldsymbol{I} + 2\mu\nabla^s\boldsymbol{u}) - \boldsymbol{f}_{sf} = \boldsymbol{0} \qquad \text{in } \Omega \tag{13}$$

$$\nabla\cdot\boldsymbol{u} - m_e\boldsymbol{n}\cdot\nabla(\frac{1}{\rho}) = 0 \qquad \text{in } \Omega \tag{14}$$

where $\boldsymbol{u}$ and p are the velocity and pressure fields, ρ is the density, μ is the dynamic viscosity, $\boldsymbol{g}$ is the gravitational acceleration, ∇^s is the symmetric gradient operator, $\boldsymbol{I}$ is a 3×3 identity tensor, and $\boldsymbol{f}_{sf}$ represents the interfacial forces that will be defined later. In this model, incompressibility (divergence-free of velocity) still holds in the metal and gas phases individually. However, compressibility is induced at the gas-metal interface due to the local evaporation, which is accounted for by the second term of the continuity equation in Eq. (14), where $\boldsymbol{n} = -\frac{\nabla\phi}{|\nabla\phi|}$ is the unit normal vector at the gas-metal interface pointing from metal phase to gas phase. One should note the definition of this normal is different from that of cloud points defined in the previous section. At last, m_e is the net evaporation mass flux rate. The formula for m_e is defined as:

$$m_e = \zeta P_{sat}(T)\sqrt{\frac{m_{mol}}{2\pi R_{gas}T}} \tag{15}$$

where the coefficient ζ accounts for the condensation effect and is set to 0.4 in this paper, m_{mol} is the molar mass of evaporating species, R_{gas} is the gas constant, P_{sat} is the saturation pressure based Clausius–Clapeyron relation, which reads

$$P_{sat}(T) = P_{amb}exp\left[\frac{-L_v m_{mol}}{R_{gas}}(\frac{1}{T} - \frac{1}{T_{evap}})\right] \tag{16}$$

where L_v is the latent heat of vaporization, T_{evap} is the boiling temperature, P_{amb} is the ambient pressure and set to 101 kPa in the metal AM simulations here. A complete derivation of Eq. (14) can be found in the last author's previous work in [48], which adopted a control volume finite element discretization. This evaporation model is also similar to those proposed in [49–52]. One should note that our approach is based on a continuum model and assumes that the Mach number of the vapor flow is very low, which is valid for the problems considered in the paper. This model cannot handle the extreme situation if the vapor escaping speed is higher than the sound speed because the continuum assumption does not hold in the Knudsen layer and the numerical interface thickness (at the scale of several micrometers) is much larger than the Knudsen layer thickness (at the scale of several mean free path). An alternative laser model that can potentially handle this situation can be found in [53].

Interfacial forces play essential roles in metal AM physics. Although the air–metal interface is recovered in the geometry-based re-initialization stage, it does not conform to the volumetric mesh, making the traction BC based on interface-tracking infeasible. Thus, the continuum surface force (CSF) model [54,55] based on interface-capturing is employed here, and four types of interfacial forces are modeled in $\boldsymbol{f}_{sf}$, which reads

$$\boldsymbol{f}_{sf} = \boldsymbol{f}_\sigma + \boldsymbol{f}_m + \boldsymbol{f}_e + \boldsymbol{f}_r \tag{17}$$

where $\boldsymbol{f}_\sigma$ and $\boldsymbol{f}_m$ are the surface tension and Marangoni force, defined as

$$\boldsymbol{f}_\sigma = \delta_\rho\sigma\overline{\kappa}\boldsymbol{n} \tag{18}$$

$$\boldsymbol{f}_m = \delta_\rho\frac{\partial\sigma}{\partial T}\left[\nabla T - \boldsymbol{n}(\boldsymbol{n}\cdot\nabla T)\right] \tag{19}$$

where $\sigma = \sigma_0 + \frac{\partial \sigma}{\partial T}(T - T_0)$ is the surface tension coefficient, where σ_0 is surface tension coefficient at the reference temperature T_0, $\frac{\partial \sigma}{\partial T}$ is the Marangoni coefficient, $\delta_\rho = (\frac{2\rho}{\rho_m + \rho_g})\frac{\partial H}{\partial \phi}$ is a density-scaled Dirac delta function. $\overline{\kappa} = -\nabla \cdot \boldsymbol{n}$ is the mean curvature of the gas–metal interface. Calculating $\overline{\kappa}$ needs the second-order differentiation of ϕ, the evaluation of which at quadrature points necessitates a L_2 projection if linear tetrahedron elements are employed in spatial discretization. The projection can be avoided if higher-order basis functions, such as isogeometric basis functions [56,57], are adopted [43].

$\boldsymbol{f}_e$ and $\boldsymbol{f}_r$ account for the evaporation force and recoil pressure, which reads

$$\boldsymbol{f}_e = \nabla(\frac{m_e^2}{\rho}) \tag{20}$$

$$\boldsymbol{f}_r = -\delta_\rho P_{recoil} \boldsymbol{n} \tag{21}$$

where P_{recoil} is the recoil pressure, defined as

$$P_{recoil} = 0.54 P_{sat} \tag{22}$$

2.2.3. Energy equation

The temperature field satisfies the following conservation law of enthalpy.

$$\rho c_p \frac{\partial T}{\partial t} + \rho c_p \boldsymbol{u} \cdot \nabla T + \rho L_m \frac{\partial f_l}{\partial t} + \rho L_m \boldsymbol{u} \cdot \nabla f_l - \nabla \cdot (\kappa \nabla T) - Q_{sf} = 0 \tag{23}$$

where c_p is the specific heat, L_m is the latent heat of fusion, κ is the thermal conductivity, Q_{sf} is the energy source term handled by a CSF model, which consists of three parts, namely,

$$Q_{sf} = Q_r + Q_e + Q_l \tag{24}$$

where Q_r accounts for the radiative cooling, defined as

$$Q_r = -\delta_\rho \sigma_{sb} \epsilon (T^4 - T_0^4) \tag{25}$$

where σ_{sb} is the Stefan–Boltzmann constant, ϵ is the material emissivity. Q_e accounts for the evaporative cooling, defined as

$$Q_e = -\delta_\rho L_v m_e \tag{26}$$

At last, Q_l accounts for the heat source, defined as.

$$Q_l = \delta_\rho I_s \tag{27}$$

where I_s is the equivalent laser ray energy after considering the multiple reflections. The definition is described in the next section.

2.3. Ray tracing for multiple laser reflections

Metal AM processes involve violent laser-material interactions. In particular, the multiple laser reflections are vital factors that determine the temperature and melt pool evolution. They must be evaluated carefully to achieve accurate AM process prediction. To this end, a ray-tracing technique is presented [58–62]. The laser is uniformly decomposed into N_{ray} rays first. The initial energy of each ray is computed by

$$I_i^0 = \int_{A_i} I(\boldsymbol{x}) dS \tag{28}$$

where i in the ray index, A_i is the area underneath the ray, and $I(\boldsymbol{x})$ is the distribution of original laser, taking a Gaussian profile as

$$I(\boldsymbol{x}) = \frac{2Q\eta}{\pi r_b^2} exp\left[\frac{-2|\boldsymbol{x} - \boldsymbol{x}_0|^2}{r_b^2}\right] \tag{29}$$

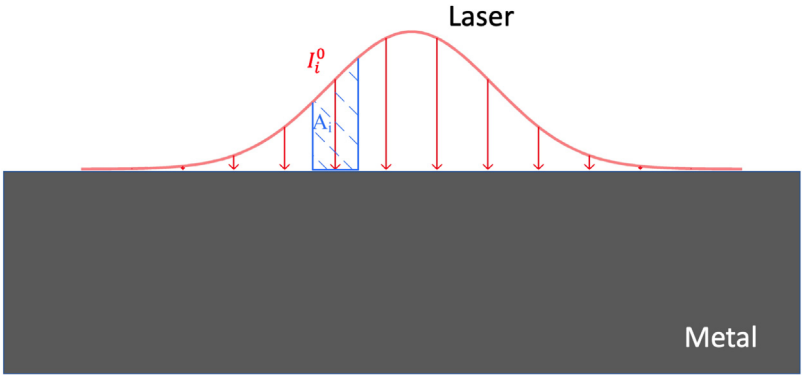

Fig. 4. The laser decomposition into multiple rays.

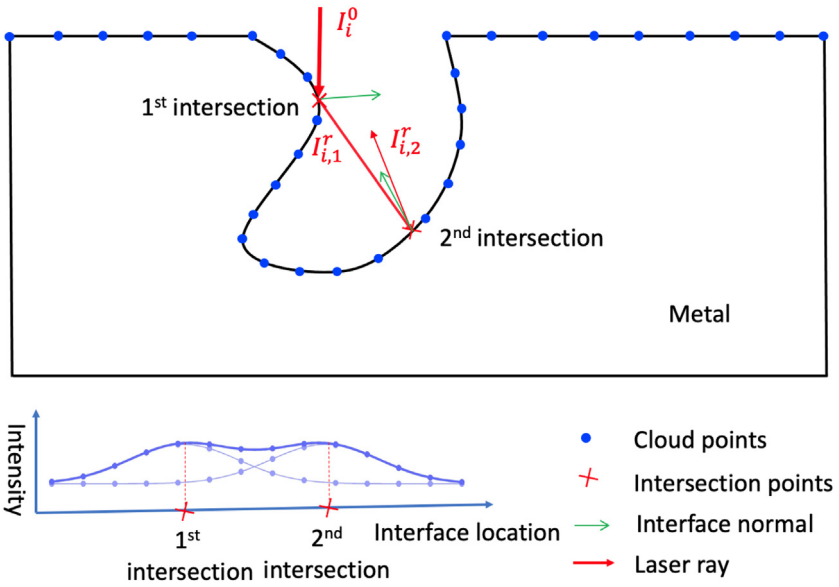

Fig. 5. 2D description of the ray tracing and laser model.

where Q is the laser power, r_b is the beam radius, η is the laser absorption coefficient, $\boldsymbol{x}_0$ is the laser center. Fig. 4 sketches a 2D description of the decomposition.

For each ray, we trace all the intersection points between it and the gas-metal interface during the multiple reflections process. Identifying these intersections can also be accelerated by taking advantage of the octree structure of the triangulated surface. The procedure is presented as follows, and a 2D description is shown in Fig. 5, in which a ray has two intersections with the gas-metal interface. Let N_i denote the number of intersections between the ith ray and the gas-metal interface. For the jth ($j = 1, 2, \ldots, N_i$) intersection, the absorbed ray energy, denoted by I_{ij}^a, and the reflected ray energy, denoted by I_{ij}^r, are computed as

$$I_{i,j}^a = \alpha(\theta) cos(\theta) I_{i,j-1}^r \tag{30}$$

$$I_{i,j}^r = [1 - \alpha(\theta)]\, cos(\theta) I_{i,j-1}^r \tag{31}$$

These two recursive relationships imply that the current absorbed and reflected energy come from the ray reflected from the previous intersection. Thus, $I_{i,0}^r = I_i^0$. The distribution of absorbed and reflected energy depends on the

incident angle θ and a ray absorption coefficient, also a function of θ, defined as

$$\alpha(\theta) = 1 - \frac{1}{2}\left[\frac{1+(1-\epsilon cos\theta)^2}{1+(1+\epsilon cos\theta)^2} + \frac{\epsilon^2 - 2\epsilon cos\theta + 2cos\theta^2}{\epsilon^2 + 2\epsilon cos\theta + 2cos\theta^2}\right] \tag{32}$$

where ϵ is a material constant associated with the material's electrical conductance.

For each intersection, the absorbed ray energy is distributed on the gas-metal interface by a Gaussian profile, namely,

$$p_{i,j}(\boldsymbol{x}) = \frac{1}{2\pi\beta^2} exp^{-\frac{|\boldsymbol{x}-\boldsymbol{x}_{i,j}|^2}{2\beta^2}} \tag{33}$$

where $\boldsymbol{x}_{i,j}$ is the coordinates of the intersection, β is a length scale that is 3 times of the local element length. With the above definitions, I_s in Eq. (27) is computed by summing of the absorbed energy of all the intersections, namely,

$$I_s = \sum_{i=1}^{N_{ray}} \sum_{j=1}^{N_i} I_{i,j}^a p_{i,j} \tag{34}$$

2.4. Variational multiscale formulation

Residual-based variational multi-scale (VMS) formulation is utilized to solve the coupled thermal multi-phase flows equations in Eqs. (3), (13), (14), and (23). Let $\mathcal{V}_u$, $\mathcal{V}_p$, $\mathcal{V}_T$, and $\mathcal{V}_\phi$ denote the trial function spaces for velocity, pressure, temperature, and level set unknowns, respectively, and $\mathcal{W}_u$, $\mathcal{W}_p$, $\mathcal{W}_T$, and $\mathcal{W}_\phi$ denote test function spaces for momentum, continuity, temperature, and level set convection equations, respectively. The semi-discrete formulation based on VMS is stated as follows. Find $\boldsymbol{u} \in \mathcal{V}_u$, $p \in \mathcal{V}_p$, $T \in \mathcal{V}_T$, and $\phi \in \mathcal{V}_\phi$ such that for all $\boldsymbol{w} \in \mathcal{W}_u$, $q \in \mathcal{W}_p$, $s \in \mathcal{W}_T$, and $\eta \in \mathcal{W}_\phi$,

$$B_{\text{VMS}}(\{\boldsymbol{w}, q, s, \eta\}, \{\boldsymbol{u}, p, T, \phi\}) - F_{\text{VMS}}(\{\boldsymbol{w}, q, s, \eta\}) = 0 \tag{35}$$

where $B_{\text{VMS}}(\{\boldsymbol{w}, q, s, \eta\}, \{\boldsymbol{u}, p, T, \phi\})$ and $F_{\text{VMS}}(\{\boldsymbol{w}, q, s, \eta\})$ are given as

$$\begin{aligned}
B_{\text{VMS}}(\{\boldsymbol{w}, q, s, \eta\}, \{\boldsymbol{u}, p, T, \phi\}) = & \int_\Omega \boldsymbol{w} \cdot \rho \left[\frac{\partial \boldsymbol{u}}{\partial t} + \nabla \cdot (\boldsymbol{u} \otimes \boldsymbol{u}) - \boldsymbol{g}\right] d\Omega \\
& + \int_\Omega \nabla^s \boldsymbol{w} : \left(-p\boldsymbol{I} + 2\mu\nabla^s \boldsymbol{u}\right) d\Omega \\
& + \int_\Omega q \left[\nabla \cdot \boldsymbol{u} - m_e \boldsymbol{n} \cdot \nabla(\frac{1}{\rho})\right] d\Omega \\
& - \int_\Omega \left(\boldsymbol{u} \cdot \nabla \boldsymbol{w} + \frac{\nabla q}{\rho}\right) \cdot \boldsymbol{u}' \, d\Omega \\
& - \int_\Omega p' \nabla \cdot \boldsymbol{w} \, d\Omega + \int_\Omega \boldsymbol{w} \cdot (\boldsymbol{u}' \cdot \nabla \boldsymbol{u}) \, d\Omega \\
& - \int_\Omega \frac{\nabla \boldsymbol{w}}{\rho} : \left(\boldsymbol{u}' \otimes \boldsymbol{u}'\right) d\Omega \\
& + \int_\Omega s \left(\rho c_p \frac{\partial T}{\partial t} + \rho c_p \boldsymbol{u} \cdot \nabla T + \rho L_m \frac{\partial f_l}{\partial t} + \rho L_m \boldsymbol{u} \cdot \nabla f_l\right) d\Omega \\
& + \int_\Omega \nabla s \cdot \kappa \nabla T \, d\Omega - \int_\Omega \boldsymbol{u} \cdot \nabla s T' \, d\Omega \\
& + \int_\Omega \eta \left(\frac{\partial \phi}{\partial t} + \boldsymbol{u} \cdot \nabla \phi\right) d\Omega - \int_\Omega (\boldsymbol{u} \cdot \nabla \eta) \phi' \, d\Omega
\end{aligned} \tag{36}$$

$$F_{\text{VMS}}(\{\boldsymbol{w}, q, s, \eta\}) = \int_\Omega \boldsymbol{w} \cdot \rho \boldsymbol{f}_{sf} \, d\Omega + \int_\Omega s Q_{sf} \, d\Omega + \int_{\Gamma^{\text{N}}} \boldsymbol{w} \cdot \boldsymbol{h}_f \, d\Gamma + \int_{\Gamma^{\text{T}}} s h_T \, d\Gamma \tag{37}$$

where $\boldsymbol{h}_f$ and h_T are the applied fluid traction and heat flux. $\boldsymbol{u}'$, p', and ϕ' are the fine-scale velocity, pressure and level set, given as

$$\boldsymbol{u}' = -\tau_{\mathrm{M}} \left\{ \rho \left[\frac{\partial \boldsymbol{u}}{\partial t} + \nabla \cdot (\boldsymbol{u} \otimes \boldsymbol{u}) - \boldsymbol{g} \right] - \nabla \cdot (-p\boldsymbol{I} + 2\mu \nabla^s \boldsymbol{u}) - \boldsymbol{f}_{sf} \right\} \tag{38}$$

$$p' = -\tau_{\mathrm{C}}\, \rho \left[\nabla \cdot \boldsymbol{u} - m_e \boldsymbol{n} \cdot \nabla (\frac{1}{\rho}) \right] \tag{39}$$

$$T' = -\tau_T \left[\rho c_p (\frac{\partial T}{\partial t} + \boldsymbol{u} \cdot \nabla T) + \rho L_m (\frac{\partial f_L}{\partial t} + \boldsymbol{u} \cdot \nabla f_L) - \nabla \cdot (\kappa \nabla T) - Q_{sf} \right] \tag{40}$$

$$\phi' = -\tau_\phi \left(\frac{\partial \phi}{\partial t} + \boldsymbol{u} \cdot \nabla \phi \right) \tag{41}$$

where τ_{M}, τ_{C}, and τ_ϕ are the stabilization parameters, defined as

$$\tau_{\mathrm{M}} = \left(\frac{4}{\Delta t^2} + \frac{4\|\boldsymbol{u}\|^2}{h^2} + \frac{16\mu^2}{\rho^2 h^4} \right)^{-1/2} \tag{42}$$

$$\tau_{\mathrm{C}} = \frac{h^2}{3\tau_{\mathrm{M}}} \tag{43}$$

$$\tau_{\mathrm{T}} = \left(\frac{4}{\Delta t^2} + \frac{4\|\boldsymbol{u}\|^2}{h^2} + \frac{16\kappa^2}{\rho^2 c_p^2 h^4} \right)^{-1/2} \tag{44}$$

$$\tau_\phi = \left(\frac{4}{\Delta t^2} + \frac{4\|\boldsymbol{u}\|^2}{h^2} \right)^{-1/2} \tag{45}$$

where h is the minimum edge length of a tetrahedron element. The above formulation features an extension of the residual-based VMS of single-phase turbulent flows, first introduced in [63], to thermal multi-phase flow problems. The terms in Eq. (36) without involving fine-scale quantities are the Galerkin formulations of Navier–Stokes, temperature, and level set convection equations, respectively. The rest can be interpreted as a stabilized method for convection-dominated problems or a large eddy simulation (LES) turbulence model. More method developments and engineering applications regarding VMS and stabilized methods for fluid mechanics can be found in [64–75].

2.5. Time integration

Generalized-α method [76,77] is employed to integrate the VMS formulation in Eq. (35) in time. Without losing generality, let $\boldsymbol{R} = \left\{ \boldsymbol{R}_M,\ \boldsymbol{R}_C,\ \boldsymbol{R}_T,\ \boldsymbol{R}_\phi \right\}^T$ denote the nodal momentum, continuity, temperature, and level set residuals, $\boldsymbol{P}$ denote the nodal pressure unknowns, and $\boldsymbol{X} = \left\{ \boldsymbol{u},\ \boldsymbol{T},\ \boldsymbol{\phi} \right\}^T$ and $\dot{\boldsymbol{X}} = \left\{ \dot{\boldsymbol{u}},\ \dot{\boldsymbol{T}},\ \dot{\boldsymbol{\phi}} \right\}^T$ denote the nodal velocity, temperature, and level set field unknowns, and their time derivatives. When stepping from t_n to t_{n+1}, $\boldsymbol{X}$ and $\dot{\boldsymbol{X}}$ are linked by the following Newmark-β scheme [78]

$$\boldsymbol{X}_{n+1} = \boldsymbol{X}_n + \Delta t \left[(1-\gamma) \dot{\boldsymbol{X}}_n + \gamma \dot{\boldsymbol{X}}_{n+1} \right] \tag{46}$$

The reason for separating pressure unknowns from others is that the residual $\boldsymbol{R}$ is evaluated at t_{n+1} for pressure but intermediate states between t_n and t_{n+1} for velocity, temperature, and level set. These intermediate states, $\boldsymbol{X}_{n+\alpha_f}$ and $\dot{\boldsymbol{X}}_{n+\alpha_m}$, are computed as

$$\dot{\boldsymbol{X}}_{n+\alpha_m} = \alpha_m \dot{\boldsymbol{X}}_{n+1} + (1-\alpha_m)\, \dot{\boldsymbol{X}}_n \tag{47}$$

$$\boldsymbol{X}_{n+\alpha_f} = \alpha_f \boldsymbol{X}_{n+1} + (1-\alpha_f) \boldsymbol{X}_n \tag{48}$$

In Eqs. (46)–(48), γ, α_m, and α_f are the parameters of Newmark-β and generalized-α methods, chosen based on the unconditional stability and second-order accuracy and requirements [76]. With the above definitions, the time integration leads to the following nonlinear equations

$$\boldsymbol{R}(\dot{\boldsymbol{X}}_{n+\alpha_m}, \boldsymbol{P}_{n+1}) = \left\{ \begin{matrix} \boldsymbol{R}_M \\ \boldsymbol{R}_C \\ \boldsymbol{R}_T \\ \boldsymbol{R}_\phi \end{matrix} \right\}_{(\dot{\boldsymbol{X}}_{n+\alpha_m}, \boldsymbol{P}_{n+1})} = \boldsymbol{0} \tag{49}$$

The above linear systems are solved in a fully coupled fashion by Newton's method, which results in the following two-stage predictor/multicorrector algorithm with a generalized minimal residual solver (GMRES) enhanced with a recursive preconditioning.

Predictor stage:

$$\dot{\boldsymbol{X}}^0_{n+1} = \frac{\gamma - 1}{\gamma}\dot{\boldsymbol{X}}_n \tag{50}$$

$$\boldsymbol{X}^0_{n+1} = \boldsymbol{X}_n \tag{51}$$

$$P^0_{n+1} = P_n \tag{52}$$

where superscript 0 indicates the quantities are initial guesses.

Multicorrector stage: Repeat the following procedure until the reduction of the norm of $\boldsymbol{R}$ satisfies the tolerance.

Step 1. Evaluate intermediate states

$$\dot{\boldsymbol{X}}^l_{n+\alpha_m} = \alpha_m \dot{\boldsymbol{X}}^l_{n+1} + (1-\alpha_m)\,\dot{\boldsymbol{X}}_n \tag{53}$$

$$\boldsymbol{X}^l_{n+\alpha_f} = \alpha_f \boldsymbol{X}^l_{n+1} + \left(1-\alpha_f\right)\boldsymbol{X}_n \tag{54}$$

where l is a Newton-iteration counter.

Step 2. Use the intermediate states to evaluate the residuals and the corresponding Jacobian matrix, which leads to the following linear systems.

$$\begin{Bmatrix} \frac{\partial \boldsymbol{R}_l}{\partial \dot{\boldsymbol{X}}_{n+1}} \\ \frac{\partial \boldsymbol{R}_l}{\partial \boldsymbol{P}_{n+1}} \end{Bmatrix} \begin{Bmatrix} \Delta \dot{\boldsymbol{X}}^l_{n+1} \\ \Delta \boldsymbol{P}^l_{n+1} \end{Bmatrix} = -\boldsymbol{R}_l(\dot{\boldsymbol{X}}^l_{n+\alpha_m}, \boldsymbol{P}^l_{n+1}) \tag{55}$$

The above linear equations are solved to get the increments: $\Delta \dot{\boldsymbol{X}}^l_{n+1}$ and $\Delta \boldsymbol{P}^l_{n+1}$.

Step 3. Correct the solutions with $\Delta \dot{\boldsymbol{X}}^l_{n+1}$ and $\Delta \boldsymbol{P}^l_{n+1}$ as follows

$$\dot{\boldsymbol{X}}^{l+1}_{n+1} = \dot{\boldsymbol{X}}^l_{n+1} + \Delta \dot{\boldsymbol{X}}^l_{n+1} \tag{56}$$

$$\boldsymbol{X}^{l+1}_{n+1} = \boldsymbol{X}^l_{n+1} + \gamma \Delta t \Delta \dot{\boldsymbol{X}}^l_{n+1} \tag{57}$$

$$\boldsymbol{P}^{l+1}_{n+1} = \boldsymbol{P}^l_{n+1} + \Delta \boldsymbol{P}^l_{n+1} \tag{58}$$

2.6. Fully-coupled linear solver and recursive preconditioning

The multicorrector stage requires the solution of a large linear system given by Eq. (55), which couples different components of the VMS formulation. To increase the formulation's robustness, Eq. (55) is solved by a fully coupled approach, in which the Jacobian matrix is constructed with all the terms in the VMS represented. For simplicity, we neglect the time step and iteration counts in the notation and write the Jacobian matrix as

$$\boldsymbol{J} = \begin{Bmatrix} \frac{\partial \boldsymbol{R}}{\partial \dot{\boldsymbol{X}}} \\ \frac{\partial \boldsymbol{R}}{\partial \boldsymbol{P}} \end{Bmatrix} = \begin{Bmatrix} \frac{\partial \boldsymbol{R}_M}{\partial \dot{\boldsymbol{u}}} & \frac{\partial \boldsymbol{R}_M}{\partial \boldsymbol{p}} & \frac{\partial \boldsymbol{R}_M}{\partial \dot{\boldsymbol{T}}} & \frac{\partial \boldsymbol{R}_M}{\partial \dot{\boldsymbol{\phi}}} \\ \frac{\partial \boldsymbol{R}_C}{\partial \dot{\boldsymbol{u}}} & \frac{\partial \boldsymbol{R}_C}{\partial \boldsymbol{p}} & \frac{\partial \boldsymbol{R}_C}{\partial \dot{\boldsymbol{T}}} & \frac{\partial \boldsymbol{R}_C}{\partial \dot{\boldsymbol{\phi}}} \\ \frac{\partial \boldsymbol{R}_T}{\partial \dot{\boldsymbol{u}}} & \frac{\partial \boldsymbol{R}_T}{\partial \boldsymbol{p}} & \frac{\partial \boldsymbol{R}_T}{\partial \dot{\boldsymbol{T}}} & \frac{\partial \boldsymbol{R}_T}{\partial \dot{\boldsymbol{\phi}}} \\ \frac{\partial \boldsymbol{R}_{\boldsymbol{\phi}}}{\partial \dot{\boldsymbol{u}}} & \frac{\partial \boldsymbol{R}_{\boldsymbol{\phi}}}{\partial \boldsymbol{p}} & \frac{\partial \boldsymbol{R}_{\boldsymbol{\phi}}}{\partial \dot{\boldsymbol{T}}} & \frac{\partial \boldsymbol{R}_{\boldsymbol{\phi}}}{\partial \dot{\boldsymbol{\phi}}} \end{Bmatrix} \tag{59}$$

Due to the complexity of thermal multi-phase flow problems and large property ratios, the condition number of the above Jacobian matrix is very large. Thus, effective preconditioning is necessary. In this paper, we develop a preconditioning strategy constructed in a recursive fashion. To facilitate the derivation, let $\boldsymbol{J}_3 = \begin{Bmatrix} \frac{\partial \boldsymbol{R}_M}{\partial \dot{\boldsymbol{u}}} & \frac{\partial \boldsymbol{R}_M}{\partial \boldsymbol{p}} & \frac{\partial \boldsymbol{R}_M}{\partial \dot{\boldsymbol{T}}} \\ \frac{\partial \boldsymbol{R}_C}{\partial \dot{\boldsymbol{u}}} & \frac{\partial \boldsymbol{R}_C}{\partial \boldsymbol{p}} & \frac{\partial \boldsymbol{R}_C}{\partial \dot{\boldsymbol{T}}} \\ \frac{\partial \boldsymbol{R}_T}{\partial \dot{\boldsymbol{u}}} & \frac{\partial \boldsymbol{R}_T}{\partial \boldsymbol{p}} & \frac{\partial \boldsymbol{R}_T}{\partial \dot{\boldsymbol{T}}} \end{Bmatrix}$ denote the velocity–pressure–temperature block in $\boldsymbol{J}$, $\boldsymbol{J}_2 = \begin{Bmatrix} \frac{\partial \boldsymbol{R}_M}{\partial \dot{\boldsymbol{u}}} & \frac{\partial \boldsymbol{R}_M}{\partial \boldsymbol{p}} \\ \frac{\partial \boldsymbol{R}_C}{\partial \dot{\boldsymbol{u}}} & \frac{\partial \boldsymbol{R}_C}{\partial \boldsymbol{p}} \end{Bmatrix}$ denote the

Navier–Stokes block. Let $\boldsymbol{M}$, $\boldsymbol{M}_3$, and $\boldsymbol{M}_2$ denote the preconditioning matrices for $\boldsymbol{J}$, $\boldsymbol{J}_3$, and $\boldsymbol{J}_2$, respectively. Here $\boldsymbol{M}$ is the final preconditioning matrix, which is constructed upon the preconditioning matrix for the level set block $\frac{\partial \boldsymbol{R}_{\boldsymbol{\phi}}}{\partial \dot{\boldsymbol{\phi}}}$ and $\boldsymbol{M}_3$ in the following way

$$\boldsymbol{M} = \boldsymbol{M}_3^* + \boldsymbol{M}_\phi^* - \boldsymbol{M}_\phi^* \boldsymbol{J} \boldsymbol{M}_3^* \tag{60}$$

where $\boldsymbol{M}_3^*$ and $\boldsymbol{M}_\phi^*$ are defined as

$$\boldsymbol{M}_3^* = \begin{Bmatrix} \boldsymbol{M_3} & \boldsymbol{O} \\ \boldsymbol{O} & \boldsymbol{O} \end{Bmatrix} \tag{61}$$

and

$$\boldsymbol{M}_\phi^* = \begin{Bmatrix} \boldsymbol{O} & \boldsymbol{O} & \boldsymbol{O} & \boldsymbol{O} \\ \boldsymbol{O} & \boldsymbol{O} & \boldsymbol{O} & \boldsymbol{O} \\ \boldsymbol{O} & \boldsymbol{O} & \boldsymbol{O} & \boldsymbol{O} \\ \boldsymbol{O} & \boldsymbol{O} & \boldsymbol{O} & \boldsymbol{M}_\phi \end{Bmatrix} \tag{62}$$

where $\boldsymbol{M}_\phi$ is a multigrid preconditioning matrix for $\frac{\partial \boldsymbol{R}_{\boldsymbol{\phi}}}{\partial \dot{\boldsymbol{\phi}}}$. It should be noted these zero blocks in $\boldsymbol{M}_3^*$ and $\boldsymbol{M}_\phi^*$ are designed to ensure that the dimensions of the matrix multiplications in Eq. (60) are consistent.

Similarly, $\boldsymbol{M}_3$ is constructed upon the preconditioning matrix for the temperature block $\frac{\partial \boldsymbol{R}_T}{\partial \dot{\boldsymbol{T}}}$ and $\boldsymbol{M}_2$ as follows.

$$\boldsymbol{M}_3 = \boldsymbol{M}_2^* + \boldsymbol{M}_T^* - \boldsymbol{M}_T^* \boldsymbol{J}_3 \boldsymbol{M}_2^* \tag{63}$$

where $\boldsymbol{M}_2^*$ and $\boldsymbol{M}_T^*$ are defined as

$$\boldsymbol{M}_2^* = \begin{Bmatrix} \boldsymbol{M_2} & \boldsymbol{O} \\ \boldsymbol{O} & \boldsymbol{O} \end{Bmatrix} \tag{64}$$

and

$$\boldsymbol{M}_T^* = \begin{Bmatrix} \boldsymbol{O} & \boldsymbol{O} & \boldsymbol{O} \\ \boldsymbol{O} & \boldsymbol{O} & \boldsymbol{O} \\ \boldsymbol{O} & \boldsymbol{O} & \boldsymbol{M}_T \end{Bmatrix} \tag{65}$$

where $\boldsymbol{M}_T$ is a multigrid preconditioning for $\frac{\partial \boldsymbol{R}_T}{\partial \dot{\boldsymbol{T}}}$.

Finally, the preconditioning matrix $\boldsymbol{M}_2$ for the Navier–Stokes block $\boldsymbol{J}_2$ is defined as

$$\boldsymbol{M}_2 = \begin{bmatrix} \boldsymbol{I} & -(\frac{\partial \boldsymbol{R}_M}{\partial \dot{\boldsymbol{u}}})^{-1}(\frac{\partial \boldsymbol{R}_M}{\partial \boldsymbol{p}}) \\ \boldsymbol{0} & \boldsymbol{I} \end{bmatrix} \begin{bmatrix} (\frac{\partial \boldsymbol{R}_M}{\partial \dot{\boldsymbol{u}}})^{-1} & \boldsymbol{0} \\ \boldsymbol{0} & \boldsymbol{S}^{-1} \end{bmatrix} \begin{bmatrix} \boldsymbol{I} & \boldsymbol{0} \\ -(\frac{\partial \boldsymbol{R}_C}{\partial \dot{\boldsymbol{u}}})(\frac{\partial \boldsymbol{R}_M}{\partial \dot{\boldsymbol{u}}})^{-1} & \boldsymbol{I} \end{bmatrix} \tag{66}$$

where $\boldsymbol{S} = (\frac{\partial \boldsymbol{R}_C}{\partial \boldsymbol{p}}) - (\frac{\partial \boldsymbol{R}_C}{\partial \dot{\boldsymbol{u}}})(\frac{\partial \boldsymbol{R}_M}{\partial \dot{\boldsymbol{u}}})^{-1}(\frac{\partial \boldsymbol{R}_M}{\partial \boldsymbol{p}})$ is the Schur complement. Inverse of matrix is obtained by solving the corresponding linear systems with GMRES. One should note that the construction of $\boldsymbol{M}_2$ is different from $\boldsymbol{M}_3$ and $\boldsymbol{M}$ because of the special structure of Navier–Stokes equations. The method for $\boldsymbol{M}_2$ is similar to the nested preconditioning presented in [79]. The choice of $\boldsymbol{M}_2$ is motivated by the fact that pressure serves as a Lagrangian multiplier in the system and $\frac{\partial \boldsymbol{R}_C}{\partial \boldsymbol{p}}$ is close to zero considering the stabilization terms are relatively small. Another preconditioning choice for $\boldsymbol{J}$ is using the inverse of each individual decoupled block for velocity–pressure, temperature, and level set blocks, which has been employed in our previous work in [41] for thermal multi-phase flows.

2.7. Mass fixing

Mass conservation is important in multi-phase flow problems [80,81]. In the current paper, global mass conservation is preserved by a mass fixing method extended from our previous work to account for the evaporated mass in metal AM problems. The residual of the global metal mass conservation equation of metal is defined as

$$\int_0^T \int_{\Gamma_I} m_e(\phi) d\Gamma dt + m_t(\phi) - m_0 \tag{67}$$

where the first integral is the accumulated evaporated metal mass, m_0 is the initial metal mass, m_t are the current metal mass in the domain, defined as

$$m_t(\phi) = \int_{\Omega} \rho_m H(\phi) d\Omega \tag{68}$$

where ρ_m is the metal density. To ensure the global mass conversation, the level set field ϕ, after convection and re-initialization, is perturbed by a global constant $\delta\phi$, the value of which is obtained by solving the following scalar equation, which recovers global mass conservation.

$$\int_0^T \int_{\Gamma_I} m_e(\phi + \delta\phi) d\Gamma dt + m_t(\phi + \delta\phi) - m_0 = 0 \tag{69}$$

One should note that the above equation is a scalar equation that can be solved efficiently. Besides, since the level set field is globally shifted by $\delta\phi$, it does not ruin the signed distance property that is recovered in the re-initialization stage.

2.8. Implementation details

The above mathematical formulation is implemented as follows.

- **Initialization**
- **Integrate over time**: For each time step, start with initial guesses and iterate the following steps until convergence.

    1. Use level set and liquid fraction to get material properties.
    2. Apply ray-tracing to get the equivalent laser energy in the heat source model.
    3. Linearize RBVMS formulation by Newton's method.
    4. Solve the linear system with the linear solver and proposed preconditioning.
    5. Update the solutions for velocity, pressure, temperature, and level set.
    6. Update liquid fraction.
    7. Update level set field with geometry-based re-initialization.
    8. Update level set field with mass-fixing.

3. Numerical examples

We test the proposed approach's accuracy and modeling capabilities on four different problems. The first two are representative benchmark problems on level set convection and bubble dynamics, aiming to compare the performance of geometry-based re-initialization and the PDE-based counterpart. The next are two metal AM simulations, aiming to assess the prediction accuracy on the key AM quantities by comparing with the experiments recently conducted by Argonne National Laboratory.

3.1. 3D Zalesak problem

The 3D Zalesak sphere problem is simulated. This is a pure level set convection problem, in which a slotted sphere with a radius of 0.15 is initialized by level set field at (0.5,0.75,0.5) in a unit cube ($[0, 1] \times [0, 1] \times [0, 1]$). The sphere is convected by the following given velocity

$$\boldsymbol{u} = \frac{\pi}{314}(0.5 - x_2, x_1 - 0.5, 0.0) \tag{70}$$

which rotates the sphere rigidly with angular velocity $\frac{\pi}{314}$ and completes one rotation every 628 non-dimensional time units.

We simulate the problem using both geometry-based and PDE-based re-initialization approaches, with precisely the same parameters for both. The PDE-based re-initialization is solved with a VMS approach with the generalize-α method for pseudo-time. The details can be found in our previous work in [43,82]. An unstructured tetrahedral mesh with uniform element length h =0.01 is used in the simulations. The simulations run for two cycles with Δt = 0.5. Fig. 6 shows the sphere shape at every quarter during the two cycles. Although both methods preserve the original shape of the slotted sphere well, a noticeable improvement can be observed from the geometry-based case, especially for the second rotation.

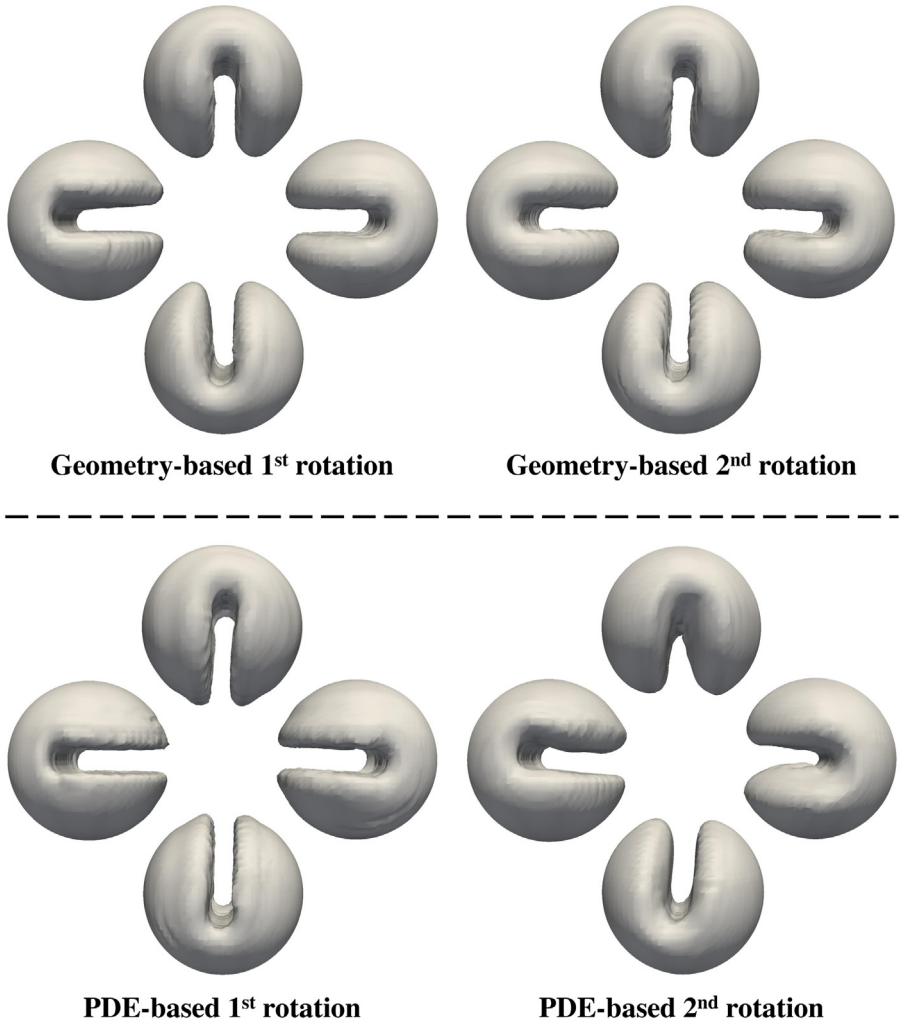

Fig. 6. Sphere shape during two cycles.

3.2. Static bubble

We then simulate a static bubble in inviscid liquid without gravity. The exact solutions of this problem are that velocity is zero and pressure difference across the bubble satisfies the following Young–Laplace equation.

$$\triangle p = \sigma \frac{2}{R} \tag{71}$$

where R is the bubble radius.

We simulate the problem in a cubic domain ($[-4, 4] \times [-4, 4] \times [-4, 4]$) with unstructured tetrahedral elements. The bubble center is located at (0,0,0). Surface tension coefficient σ is set to 73. The density ratio is $\frac{\rho_l}{\rho_g} = 1000$. No-slip boundary condition is employed for all the surfaces. A refinement study with three element lengths, $\frac{R}{h}$=5, 10, and 20, is preformed.

We report the simulated results at the 50th-time step. Figs. 7 and 8 show the pressure contour on a plane cut and along the line from $(-4, 0, 0)$ to $(4, 0, 0)$. Both methods produce an accurate prediction on the pressure difference and converge to the exact solution as the mesh is refined. Fig. 9 shows the velocity (also called parasite current in the literature) magnitude on the plane of $z = 0$. Researchers showed that using the balanced-force CSF model with hard-coded exact mean curvature reduces the velocity magnitude to zero in machine precision [83–87]. However,

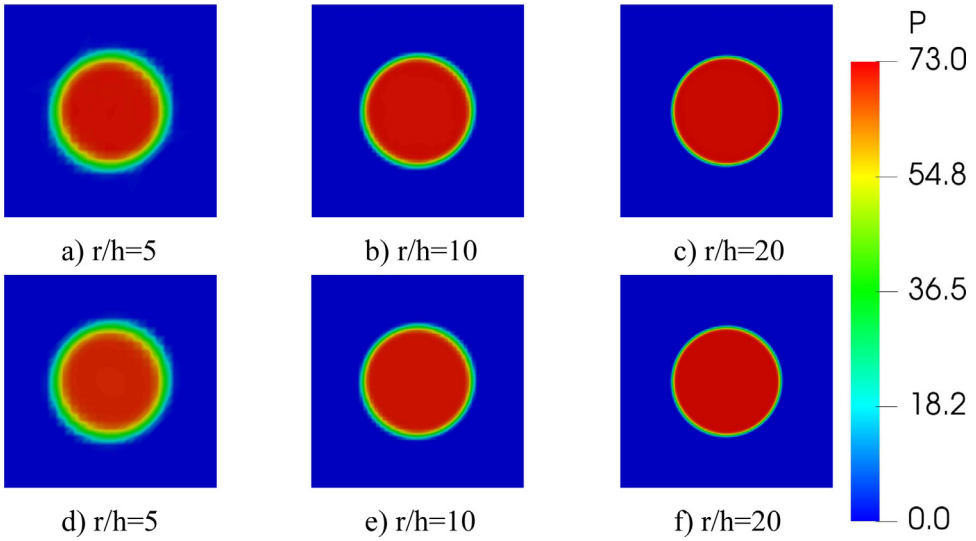

Fig. 7. Pressure contour on three meshes: Geometry-based re-initialization (top). PDE-based re-initialization (bottom). (unit: Pa).

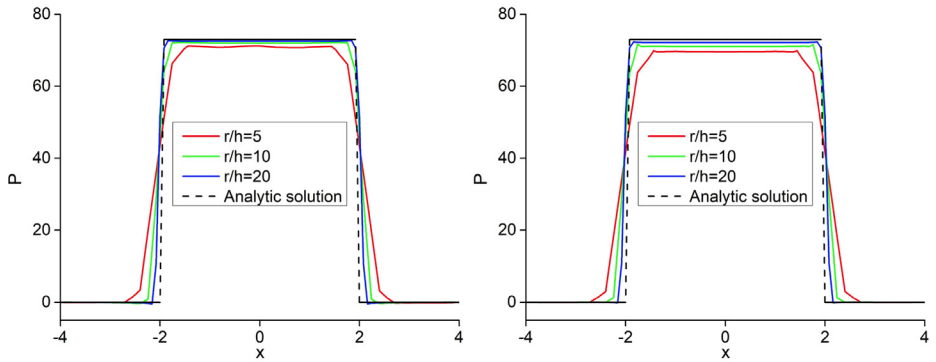

Fig. 8. Pressure along the line from $(-4, 0, 0)$ to $(4, 0, 0)$ on three meshes: Geometry-based re-initialization (left). PDE-based re-initialization (right). (unit: Pa).

given that it is impossible to obtain analytical mean curvature in real-world problems, we still employ the traditional CSF model and numerically compute the mean curvature by a L_2 projection as mentioned above. This CSF model results in non-negligible parasite currents in the domain. Nonetheless, the geometry-based re-initialization produces smaller velocity magnitudes than the PDE-based approach for the three meshes, as seen from Fig. 9.

3.3. Metal AM: Static laser case

For metal AM applications, we first simulate a stationary laser melting problem to demonstrate the modeling capabilities of phase transition and keyhole evolution. In the simulation, Argon and Ti-6Al-4V are used for the gas and metal phases, respectively, and their mechanical and thermal properties, extracted from [6,53,61,88,89], are listed in Table 1. The laser spot size and laser power are 140 μm and $Q = 156$ W. The simulation is performed on a cubic domain with unstructured tetrahedral elements. A refined region with element length $h = 3.0$ μm around the melt pool is designed to better capture the dynamics. The total number of elements and nodes are 2,466,919 and 428,566, respectively. No-penetration boundary conditions are adopted for all the outer surfaces. Dirichlet boundary conditions with room temperature are used for all the outer surfaces. The simulation runs for 2 ms with $\Delta t = 5.0 \times 10^{-7}$ s.

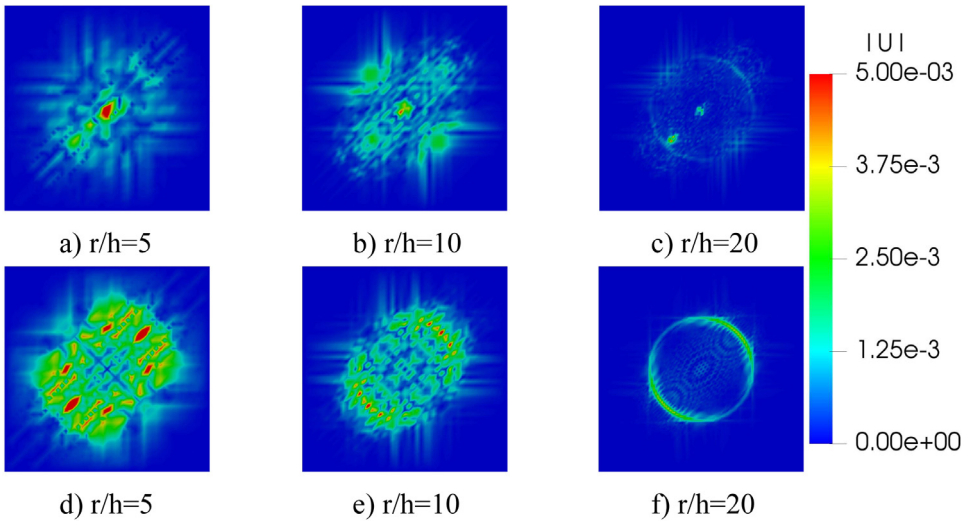

Fig. 9. Velocity magnitude on three meshes: Geometric re-initialization (top). PDE-based re-initialization (bottom). (unit: m/s).

Table 1
Mechanical properties of Ti-6Al-4V.

Name	Notation (units)	Value
Solid density	ρ_s (kg m^{-3})	4400
Liquid density	ρ_l (kg m^{-3})	4400
Gas density	ρ_s (kg m^{-3})	0.894
Solidus temperature	T_s (K)	1878
Liquid temperature	T_l (K)	1928
Boiling temperature	T_b (K)	3533
Solid specific heat capacity	c_{ps} (J kg^{-1} K^{-1})	670
Liquid specific heat capacity	c_{pl} (J kg^{-1} K^{-1})	730
Gas specific heat capacity	c_{pg} (J kg^{-1} K^{-1})	680
Solid solid conductivity	κ_s (W m^{-1} K^{-1})	21
Liquid solid conductivity	κ_l (W m^{-1} K^{-1})	29
Gas solid conductivity	κ_g (W m^{-1} K^{-1})	0.028
Latent heat of fusion	L_m (kJ kg^{-1} K^{-1})	290
Latent heat of evaporation	L_v (kJ kg^{-1} K^{-1})	9600
Solid viscosity	μ_s (Pa s)	1.0×10^{6}
Liquid viscosity	μ_l (Pa s)	5.0×10^{-3}
Gas viscosity	μ_l (Pa s)	1.5×10^{-5}
Surface tension coefficient	σ_0 (N m^{-1})	1.68
Stefan–Boltzmann constant	σ_{SB} (kg s^{-3} K^{-4})	5.67×10^{-8}
Marangoni coefficient	$\frac{\partial \gamma}{\partial T}$ (N m^{-1} K^{-1})	-2.6×10^{-4}

This problem was experimentally investigated by Argonne National Laboratory using ultrahigh-speed x-ray imaging [90]. Instead of focusing on physics discussions, here we focus on using the available quantitative experimental results to validate the simulated results and report the quantities that experiments cannot measure. Fig. 10 shows the time history of melt pool radius and penetrating depth. The melt pool radius is measured by the averaged distance from the intersection between solid–liquid/gas-metal interfaces to the laser center, while the penetrating depth is measured by the distance from the deepest point of the melt pool to the still gas–metal interface. The predicted penetrating depth shows a reasonable agreement with the experimental measurements, especially for the drilling rate in the keyhole instability stage. The simulation also generates similar keyhole shapes to the experimental images on the middle plane, as seen in Fig. 11. However, the fluctuation of penetrating depth predicted by the simulation is smaller than the experimental results, which may be related to the empirical parameters in the evaporation model.

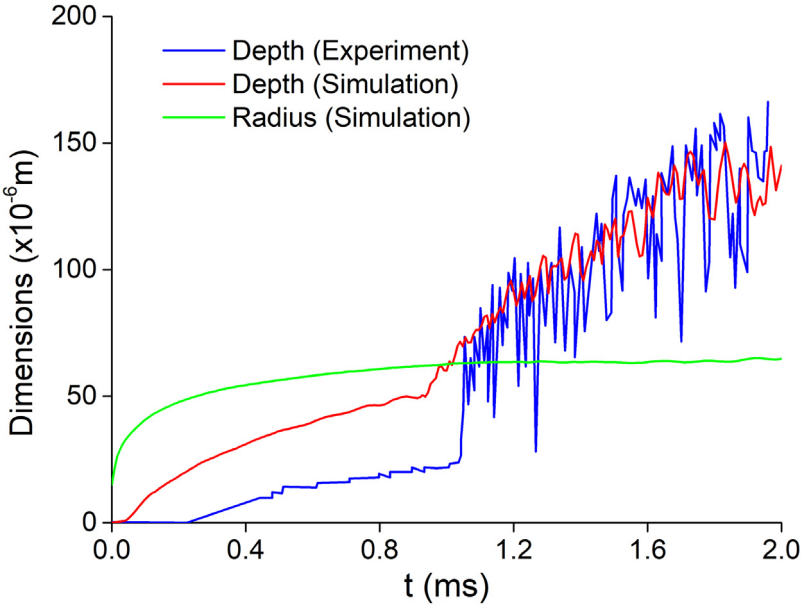

Fig. 10. Time history of melt pool depth in the stationary case.

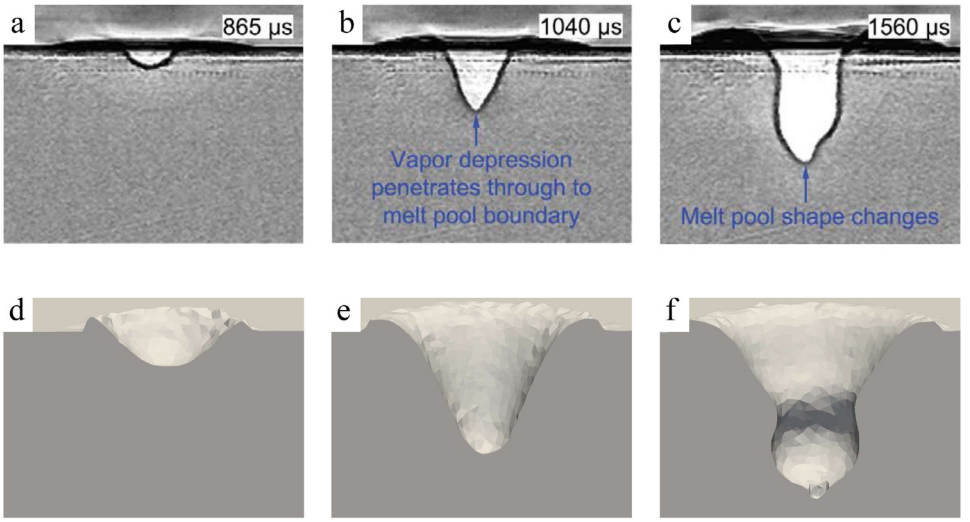

Fig. 11. Comparison of keyhole shapes in the stationary case between experimental images and current simulation. Top: experiment. Bottom: current simulation.

The following quantities that experiments cannot provide are reported. Fig. 12 depicts the temperature distribution in the metal phase and velocity vectors in the gas phase at three instances, and the corresponding volumetric distribution of ray energy (multiplied with density scaled delta function δ_s) is presented in Fig. 13. The recoil force F_z is one critical factor controlling keyhole dynamics in metal AM. In the context of interface capturing, F_z is computed as

$$F_z = -\int_{\Gamma_I} P_{recoi} d\Gamma = -\int_{\Omega} P_{recoi}\delta_s d\Omega \tag{72}$$

The time history of F_z in the keyhole instability stage is showed in Fig. 14. The magnitude and fluctuation range agrees with what was reported in [53]. Mass conversation is critical in multi-phase flows simulations. In this work,

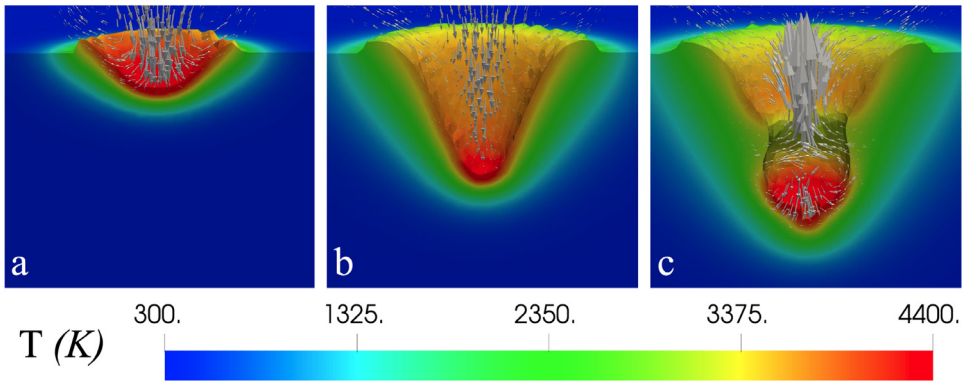

Fig. 12. Temperature in the metal phase and gas velocity vectors.

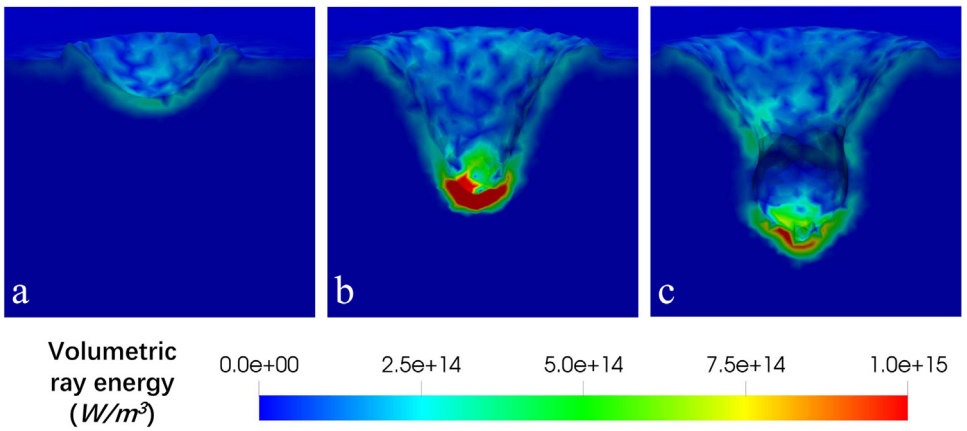

Fig. 13. Volumetric ray energy on the melt pool surface.

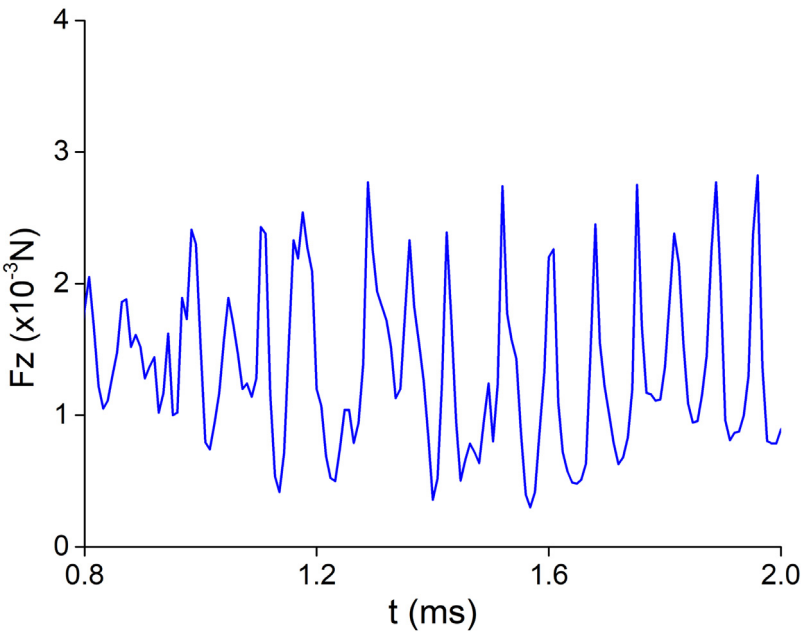

Fig. 14. Time history of recoil force F_z on the melt pool surface.

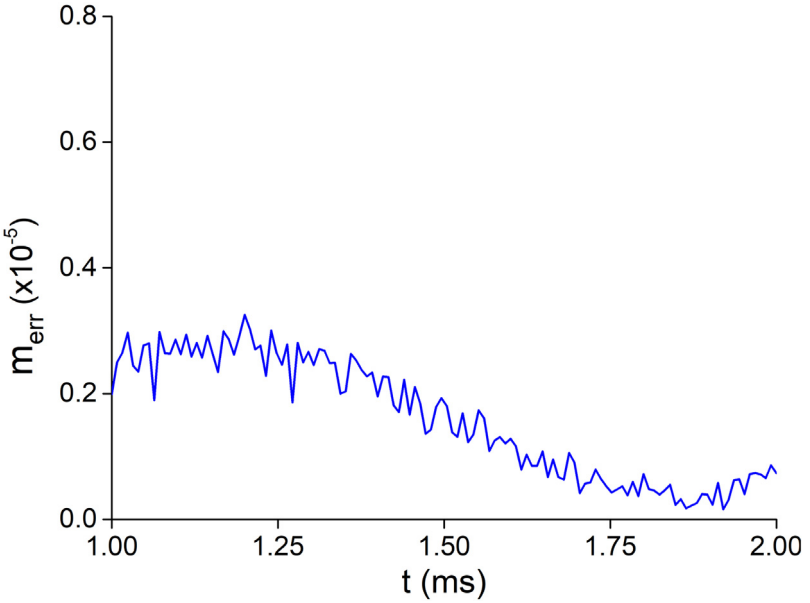

Fig. 15. Time history of relative mass conservation error.

the relative global metal mass error m_{err} is quantified as

$$m_{err} = \frac{m_0 - m_t - \int_0^T \int_{\Gamma_I} m_e d\Gamma dt}{m_0} \tag{73}$$

where m_0 is the initial metal mass, m_t is the metal mass at current time, evaluated as $m_t = \int_\Omega \rho_m H(\phi) d\Omega$, the last term in the numerator is the accumulated evaporated metal mass up to current time. The time history of m_{err} is plotted in Fig. 15, which shows the relative metal mass error is maintained at an order of 10^{-6}.

3.4. Metal AM: Moving laser case

We further test the proposed methods by simulating a moving laser case with a Ti-6Al-4V bare plate, which is also experimentally investigated in [90]. The laser spot size is 95 μm, the laser power is Q = 364 W, and the scan speed is V_s = 900 mm/s. The computation is performed in a box with a refined region around the laser track with element length h = 3 μm. The mesh has 4,215,023 elements and 612,754 nodes in total. $\Delta t = 2.5 \times 10^{-7}$ s. Fig. 16 shows the problem setup and the mesh employed in the simulation. The same types boundary condition as the stationary laser case are used.

Fig. 17 shows the time history of the melt pool dimensions. The time-averaged experimental melt pool depth [90] is also plotted for comparison. The relative discrepancy in depth between simulation and experiment is less than 10.3%. Compared with the stationary laser case, the depth fluctuation is smaller. This agrees with the trend in Argonne National Lab's latest high-speed imaging experiments [91], which found the relative fluctuation of melt pool depth decreases with increasing laser scan speed. Although the depth fluctuation is small, the keyhole instability is still pronounced, resulting in violent free surface deformation, as seen in Fig. 18, which shows the melt pool shape, temperature field in the metal, and gas velocity vectors. From Fig. 18, we also observe that the heat-induced gas velocity is more turbulent compared with the stationary laser case because of the more significant variation of interfacial forces induced by the moving laser. In particular, as we show in Fig. 19, the simulation captures the common experimentally observed chevron-type topography, primarily induced by Marangoni force, on the metal top surface. Fig. 20 shows the comparison of keyhole shapes between experimental images and the current simulated results at three time instances. Similar shapes are obtained. The averaged front keyhole wall angle predicted from the simulation is 69.8°, compared with 76.0° reported from the experiment [90].

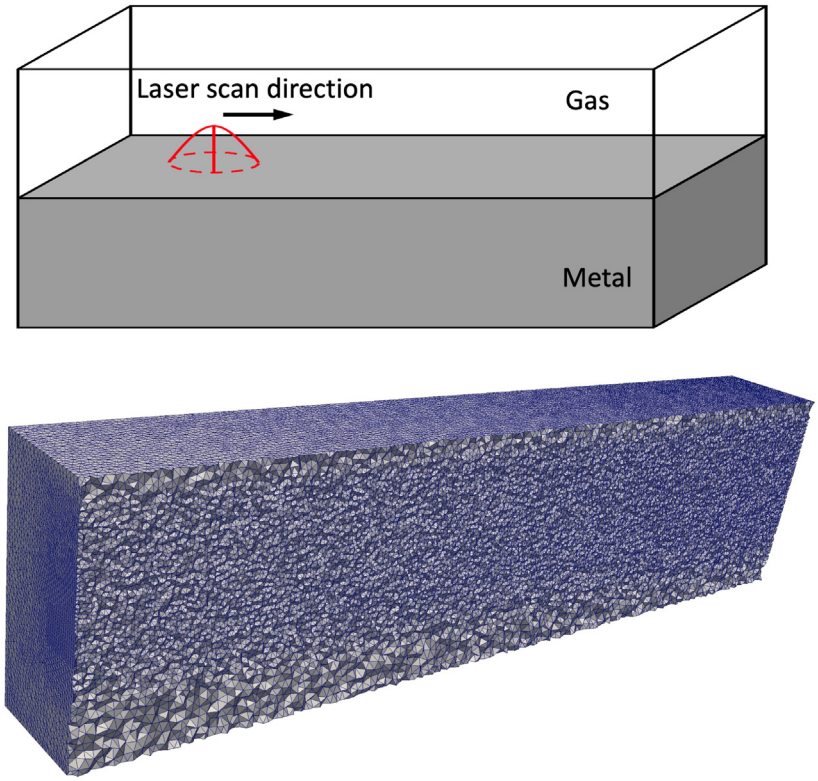

Fig. 16. Simulation setup and mesh employed in the moving laser case.

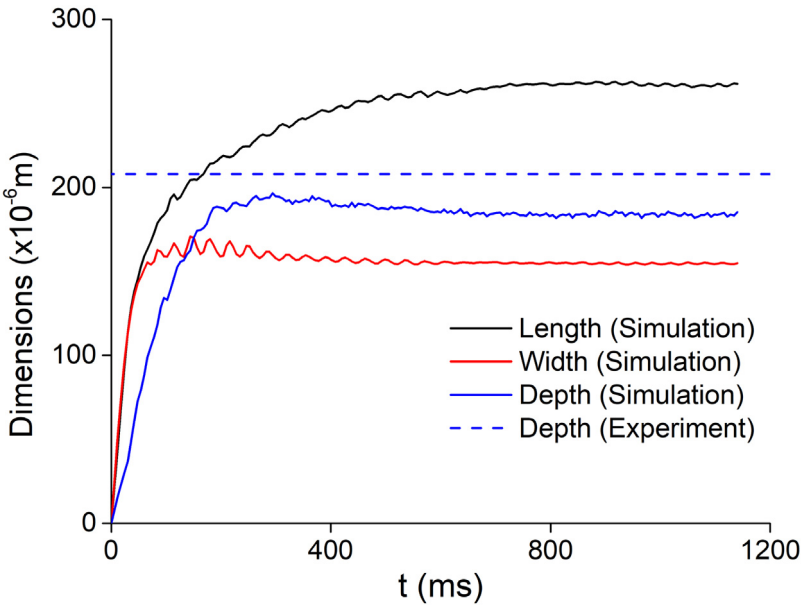

Fig. 17. Time history of melt pool dimensions in the moving laser case. The time averaged melt pool depth from [90] is plotted for comparison. The relative discrepancy in terms of depth between simulation and experiment is 10.3%.

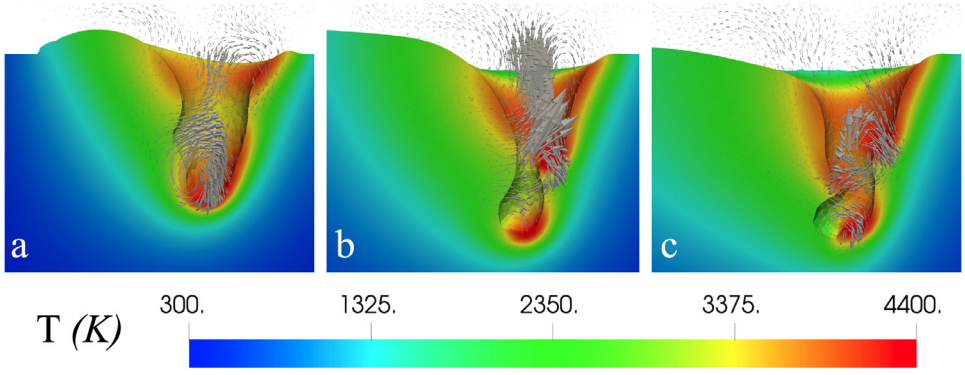

Fig. 18. Melt pool shapes, temperature in the metal, and gas velocity vectors in the moving laser case.

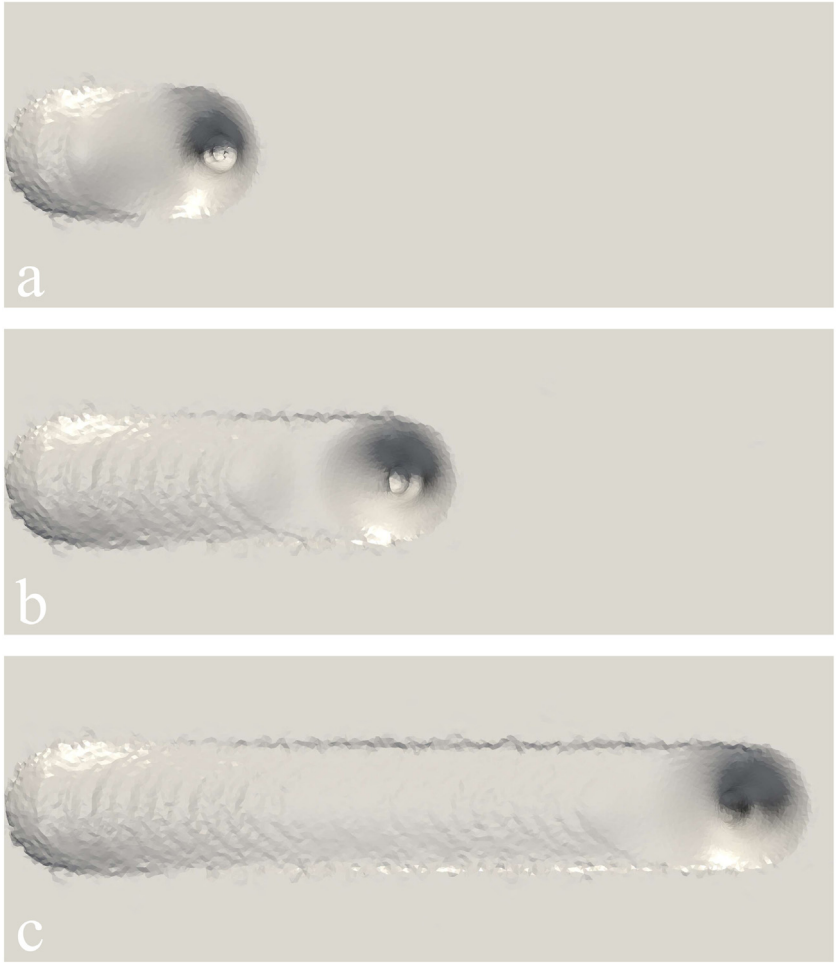

Fig. 19. Topography of metal top surface in the moving laser case.

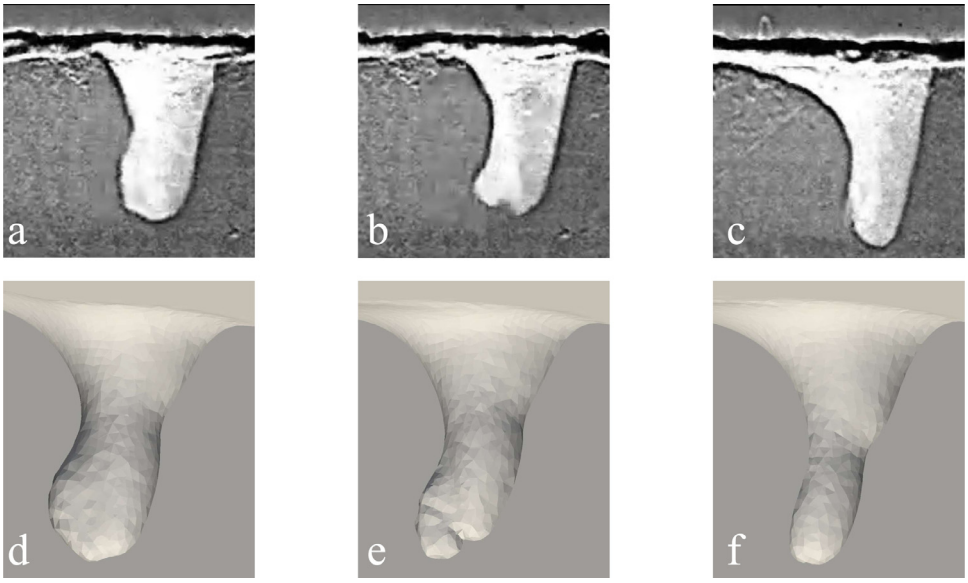

Fig. 20. Comparison of keyhole shapes between experimental images and current simulation in the moving laser case. The average front keyhole wall angle predicted from the simulation is 69.8°, compared with 76.0° from the experiment in [90].

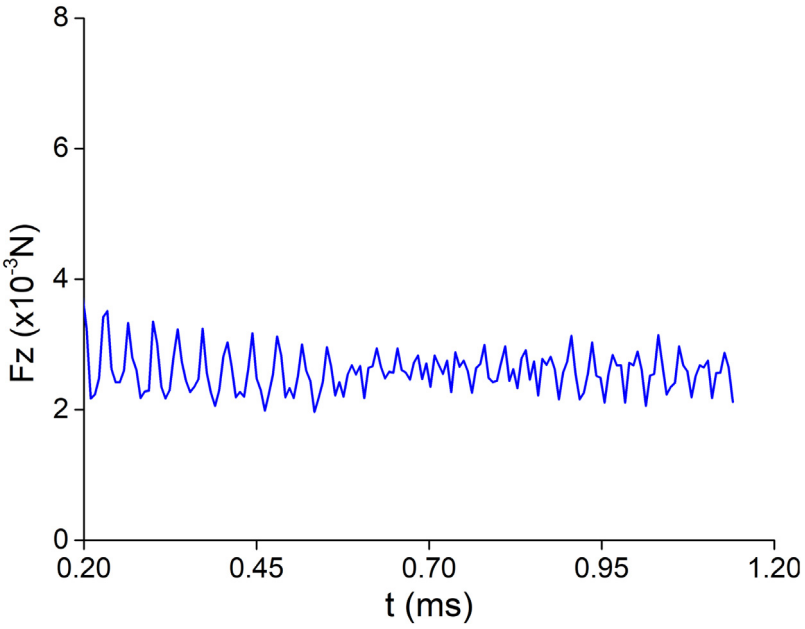

Fig. 21. Time history of recoil force F_z in the moving laser case.

Fig. 21 shows the time history of recoil force integrated over the melt pool surface. The averaged magnitude of F_z is in the same order as that of the stationary case, but with smaller fluctuation, which qualitatively explains the smaller depth fluctuation seen in Fig. 17. The time history of relative mass conservation error is in the same order as the stationary laser case, as shown in Fig. 22.

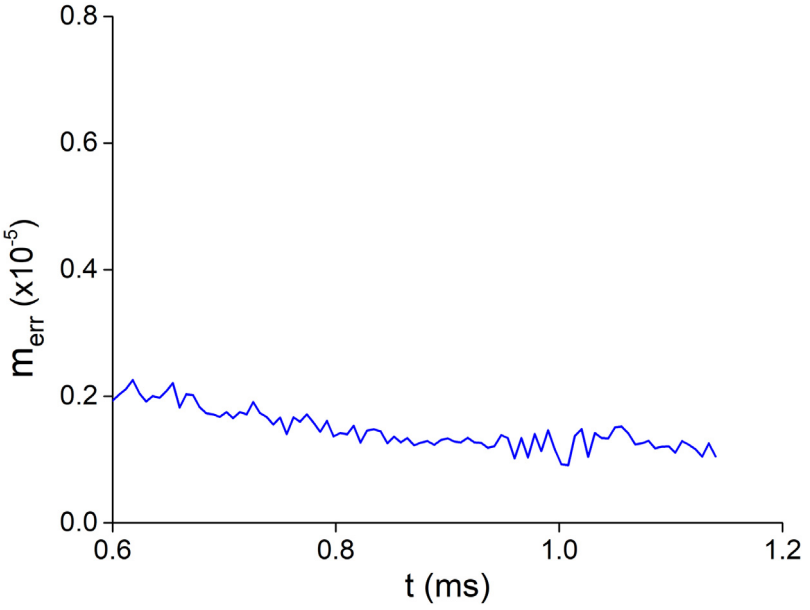

Fig. 22. Relative metal mass conservation error in the moving laser case.

4. Conclusion and future plans

In the present paper, we develop a mixed interface-capturing/interface-tracking computational thermal multi-phase flow formulation. The development aims to address the limitations of isolated interface-capturing and interface-tracking methods on metal AM process applications. The mixed formulation takes full advantages of both interface-capturing and interface-tracking methods to better handle the gas-metal interface, where AM physics, such as phase transitions and laser-material interactions, mainly occurs. Three major contributions of the paper are:

1. A simple computational geometry-based re-initialization technique, which maintains excellent signed distance property on unstructured meshes, re-constructs an explicit representation of gas-metal interface, and facilitates the treatment of the multiple laser reflections during keyhole evolution in AM processes;
2. A fully coupled VMS formulation for thermal multi-phase governing equations, including Navier-Stokes, level set convection, and thermodynamics with melting, solidification, evaporation, and interfacial force models;
3. A three-level recursive preconditioning technique to enhance the robustness of linear solvers.

We demonstrate the proposed formulation's accuracy and modeling capabilities on a set of numerical examples, including the most recent metal AM experiments performed by Argonne National Lab. The results show the great potential of the formulation in broad application in advanced manufacturing.

Some parts of the formulation can be polished, which will be addressed in the authors' subsequent development. Firstly, we will extend the geometry-based re-initialization to other spatial discretizations, such as non-uniform rational b-splines (NURBS) in IGA. Secondly, in this paper, a large portion of the mesh is pre-refined along the laser track, which can be inefficient. To this end, adaptive mesh schemes will be incorporated into the thermal multi-phase flow formulation. We will also develop efficient computational geometry algorithms to deploy the geometry-based re-initialization to adaptive meshes.

Declaration of competing interest

The authors declare that they have no known competing financial interests or personal relationships that could have appeared to influence the work reported in this paper.

References

[1] W. Frazier, Metal additive manufacturing: a review, J. Mater. Eng. Perform. 23 (6) (2014) 1917–1928.
[2] C. Noble, A. Anderson, N. Barton, J. Bramwell, A. Capps, M. Chang, J. Chou, D. Dawson, E. Diana, T. Dunn, Ale3d: An Arbitrary Lagrangian-Eulerian Multi-Physics Code, Technical Report, Lawrence Livermore National Lab.(LLNL), Livermore, CA (United States), 2017.
[3] S. Khairallah, A. Anderson, A. Rubenchik, W. King, Laser powder-bed fusion additive manufacturing: Physics of complex melt flow and formation mechanisms of pores, spatter, and denudation zones, Acta Mater. 108 (2016) 36–45.
[4] T.T. Roehling, S. Wu, S.A. Khairallah, J.D. Roehling, S.S. Soezeri, M.F. Crumb, M.J. Matthews, Modulating laser intensity profile ellipticity for microstructural control during metal additive manufacturing, Acta Mater. 128 (2017) 197–206.
[5] S. Khairallah, A. Martin, J. Lee, G. Guss, N. Calta, J. Hammons, M. Nielsen, K. Chaput, E. Schwalbach, M. Shah, G. Chapman, T. Willey, A. Rubenchik, A. Anderson, Y. Wang, M. Matthews, W. King, Controlling interdependent meso-nanosecond dynamics and defect generation in metal 3d printing, Science 368 (6491) (2020) 660–665.
[6] W. Yan, W. Ge, Y. Qian, S. Lin, B. Zhou, W.K. Liu, F. Lin, G.J. Wagner, Multi-physics modeling of single/multiple-track defect mechanisms in electron beam selective melting, Acta Mater. 134 (2017) 324–333.
[7] W. Yan, Y. Qian, W. Ge, S. Lin, W.K. Liu, F. Lin, G.J. Wagner, Meso-scale modeling of multiple-layer fabrication process in selective electron beam melting: inter-layer/track voids formation, Mater. Des. 141 (2018) 210–219.
[8] W. Yan, S. Lin, O. Kafka, Y. Lian, C. Yu, Z. Liu, J. Yan, S. Wolff, H. Wu, E. Ndip-Agbor, M. Mozaffar, K. Ehmann, J. Cao, G. Wagner, W. Liu, Data-driven multi-scale multi-physics models to derive process–structure–property relationships for additive manufacturing, Comput. Mech. 61 (5) (2018) 521–541.
[9] W. Yan, W. Ge, J. Smith, S. Lin, O. Kafka, F. Lin, W. Liu, Multi-scale modeling of electron beam melting of functionally graded materials, Acta Mater. 115 (2016) 403–412.
[10] H. Chen, W. Yan, Spattering and denudation in laser powder bed fusion process: multiphase flow modelling, Acta Mater. (2020).
[11] C. Panwisawas, C. Qiu, M.J. Anderson, Y. Sovani, R.P. Turner, M.M. Attallah, J.W. Brooks, H.C. Basoalto, Mesoscale modelling of selective laser melting: Thermal fluid dynamics and microstructural evolution, Comput. Mater. Sci. 126 (2017) 479–490.
[12] S. Lin, Numerical Methods and High Performance Computing for Modeling Metallic Additive Manufacturing Processes at Multiple Scales PhD thesis, Northwestern University, 2019.
[13] S. Lin, Z. Gan, J. Yan, G. Wagner, A conservative level set method on unstructured meshes for modeling multiphase thermo-fluid flow in additive manufacturing processes, Comput. Methods Appl. Mech. Engrg. 372 (2020) 113348.
[14] X. Li, C. Zhao, T. Sun, W. Tan, Revealing transient powder-gas interaction in laser powder bed fusion process through multi-physics modeling and high-speed synchrotron x-ray imaging, Addit. Manuf. (2020) 101362.
[15] H. Wei, T. Mukherjee, W. Zhang, J. Zuback, G. Knapp, A. De, T. DebRoy, Mechanistic models for additive manufacturing of metallic components, Prog. Mater. Sci. (2020) 100703.
[16] T.J.R. Hughes, W.K. Liu, T.K. Zimmermann, Lagrangian–eulerian finite element formulation for incompressible viscous flows, Comput. Methods Appl. Mech. Engrg. 29 (1981) 329–349.
[17] S.O. Unverdi, G. Tryggvason, A front-tracking method for viscous, incompressible, multi-fluid flows, J. Comput. Phys. 100 (1) (1992) 25–37.
[18] J.P. Best, The formation of toroidal bubbles upon the collapse of transient cavities, J. Fluid Mech. 251 (1993) 79–107.
[19] T.E. Tezduyar, M. Behr, J. Liou, A new strategy for finite element computations involving moving boundaries and interfaces – the deforming-spatial-domain/space–time procedure: I. the concept and the preliminary numerical tests, Comput. Methods Appl. Mech. Engrg. 94 (3) (1992) 339–351.
[20] I. Güler, M. Behr, T. Tezduyar, Parallel finite element computation of free-surface flows, Comput. Mech. 23 (2) (1999) 117–123.
[21] M. Sussman, P. Smereka, S. Osher, A level set approach for computing solutions to incompressible two-phase flow, J. Comput. Phys. 114 (1) (1994) 146–159.
[22] S. Osher, J.A. Sethian, Fronts propagating with curvature-dependent speed: algorithms based on hamilton-jacobi formulations, J. Comput. Phys. 79 (1) (1988) 12–49.
[23] E. Shirani, N. Ashgriz, J. Mostaghimi, Interface pressure calculation based on conservation of momentum for front capturing methods, J. Comput. Phys. 203 (1) (2005) 154–175.
[24] C.W. Hirt, B.D. Nichols, Volume of fluid (vof) method for the dynamics of free boundaries, J. Comput. Phys. 39 (1981) 201–225.
[25] D. Jacqmin, Calculation of two-phase navier–stokes flows using phase-field modeling, J. Comput. Phys. 155 (1) (1999) 96–127.
[26] J. Bueno, H. Gomez, Liquid-vapor transformations with surfactants. Phase-field model and isogeometric analysis, J. Comput. Phys. 321 (2016) 797–818.
[27] J. Liu, C. Landis, H. Gomez, T. Hughes, Liquid–vapor phase transition: Thermomechanical theory, entropy stable numerical formulation, and boiling simulations, Comput. Methods Appl. Mech. Engrg. 297 (2015) 476–553.
[28] J. Liu, H. Gomez, J. Evans, T. Hughes, Landis, Functional entropy variables: a new methodology for deriving thermodynamically consistent algorithms for complex fluids, with particular reference to the isothermal navier–stokes–korteweg equations, J. Comput. Phys. 248 (2013) 47–86.
[29] S. Mukherjee, H. Gomez, Flow and mixing dynamics of phase-transforming multicomponent fluids, Appl. Phys. Lett. 115 (10) (2019) 104101.
[30] H. Gómez, V.M. Calo, Y. Bazilevs, T. Hughes, Isogeometric analysis of the cahn–hilliard phase-field model, Comput. Methods Appl. Mech. Engrg. 197 (49–50) (2008) 4333–4352.
[31] B. Gonzalez-Ferreiro, H. Gomez, I. Romero, A thermodynamically consistent numerical method for a phase field model of solidification, Commun. Nonlinear Sci. Numer. Simul. 19 (7) (2014) 2309–2323.

[32] P. Yue, J.J. Feng, C. Liu, J. Shen, A diffuse-interface method for simulating two-phase flows of complex fluids, J. Fluid Mech. 515 (2004) 293–317.
[33] L. Amaya-Bower, T. Lee, Single bubble rising dynamics for moderate reynolds number using lattice boltzmann method, Comput. & Fluids 39 (7) (2010) 1191–1207.
[34] S. Nagrath, K.E. Jansen, R.T. Lahey, Computation of incompressible bubble dynamics with a stabilized finite element level set method, Comput. Methods Appl. Mech. Engrg. 194 (42) (2005) 4565–4587.
[35] M.K. Tripathi, K.C. Sahu, R. Govindarajan, Dynamics of an initially spherical bubble rising in quiescent liquid, Nat. Commun. 6 (2015).
[36] M. van Sint Annaland, N.G. Deen, J.A.M. Kuipers, Numerical simulation of gas bubbles behaviour using a three-dimensional volume of fluid method, Chem. Eng. Sci. 60 (11) (2005) 2999–3011.
[37] J.M. Gimenez, N.M. Nigro, S.R. Idelsohn, E. Oñate, Surface tension problems solved with the particle finite element method using large time-steps, Comput. & Fluids (2016).
[38] R. Calderer, L. Zhu, R. Gibson, A. Masud, Residual-based turbulence models and arbitrary lagrangian–eulerian framework for free surface flows, Math. Models Methods Appl. Sci. 25 (12) (2015) 2287–2317.
[39] L. Zhu, S. Goraya, A. Masud, A stabilized interface capturing method for large amplitude breaking waves, J. Eng. Mech. (2019).
[40] K. Hong, D. Weckman, A. Strong, W. Zheng, Vorticity based turbulence model for thermofluids modelling of welds, Sci. Technol. Weld. Join. 8 (5) (2003) 313–324.
[41] J. Yan, W. Yan, S. Lin, G.J. Wagner, A fully coupled finite element formulation for liquid–solid–gas thermo-fluid flow with melting and solidification, Comput. Methods Appl. Mech. Engrg. 336 (2018) 444–470.
[42] Q. Zhu, F. Xu, S. Xu, M. Hsu, J. Yan, An immersogeometric formulation for free-surface flows with application to marine engineering problems, Comput. Methods Appl. Mech. Engrg. 361 (2020) 112748.
[43] J. Yan, S. Lin, Y. Bazilevs, G.J. Wagner, Isogeometric analysis of multi-phase flows with surface tension and with application to dynamics of rising bubbles, Comput. & Fluids 179 (2019) 777–789.
[44] I. Akkerman, Y. Bazilevs, C.E. Kees, M.W. Farthing, Isogeometric analysis of free-surface flow, J. Comput. Phys. 230 (11) (2011) 4137–4152.
[45] R.F. Ausas, E.A. Dari, G.C. Buscaglia, A geometric mass-preserving redistancing scheme for the level set function, Int. J. Numer. Methods Fluids 65 (8) (2011) 989–1010.
[46] J. Strain, Fast tree-based redistancing for level set computations, J. Comput. Phys. 152 (2) (1999) 664–686.
[47] J. Liu, J. Yan, S. Lo, A new insertion sequence for incremental delaunay triangulation, Acta Mech. Sinica 29 (1) (2013) 99–109.
[48] S. Lin, Z. Gan, J. Yan, G. Wagner, A conservative level set method on unstructured meshes for modeling multiphase thermo-fluid flow in additive manufacturing processes, Comput. Methods Appl. Mech. Engrg. 372 (2020) 113348.
[49] M. Courtois, M. Carin, P. Le Masson, S. Gaied, M. Balabane, A new approach to compute multi-reflections of laser beam in a keyhole for heat transfer and fluid flow modelling in laser welding, J. Phys. D: Appl. Phys. 46 (50) (2013) 505305.
[50] M. Courtois, M. Carin, P. Le Masson, S. Gaied, M. Balabane, Complete heat and fluid flow modeling of keyhole formation and collapse during spot laser welding, in: International Congress on Applications of Lasers & Electro-Optics, Vol. 2013, Laser Institute of America, 2013, pp. 77–84.
[51] M. Courtois, M. Carin, P. Le Masson, S. Gaied, M. Balabane, A complete model of keyhole and melt pool dynamics to analyze instabilities and collapse during laser welding, J. Laser Appl. 26 (4) (2014) 042001.
[52] A. Esmaeeli, G. Tryggvason, Computations of film boiling. part i: numerical method, Int. J. Heat Mass Transfer 47 (25) (2004) 5451–5461.
[53] L. Wang, Y. Zhang, W. Yan, Evaporation model for keyhole dynamics during additive manufacturing of metal, Phys. Rev. A 14 (6) (2020) 064039.
[54] J. Brackbill, D. Kothe, C. Zemach, A continuum method for modeling surface tension, J. Comput. Phys. 100 (2) (1992) 335–354.
[55] K. Yokoi, A density-scaled continuum surface force model within a balanced force formulation, J. Comput. Phys. 278 (2014) 221–228.
[56] J.A. Cottrell, T.J.R. Hughes, Y. Bazilevs, Isogeometric Analysis. Toward Integration of CAD and FEA, Wiley, 2009.
[57] T.J.R. Hughes, J.A. Cottrell, Y. Bazilevs, Isogeometric analysis: cad, finite elements, nurbs, exact geometry, and mesh refinement, Comput. Methods Appl. Mech. Engrg. 194 (2005) 4135–4195.
[58] W. Devesse, D. De Baere, P. Guillaume, Modeling of laser beam and powder flow interaction in laser cladding using ray-tracing, J. Laser Appl. 27 (S2) (2015) S29208.
[59] B. Liu, G. Fang, L. Lei, W. Liu, A new ray tracing heat source model for mesoscale cfd simulation of selective laser melting (slm), Appl. Math. Model. 79 (2020) 506–520.
[60] S. Han, J. Ahn, S. Na, A study on ray tracing method for cfd simulations of laser keyhole welding: progressive search method, Weld. World 60 (2) (2016) 247–258.
[61] W. Tan, N.S. Bailey, Y.C. Shin, Investigation of keyhole plume and molten pool based on a three-dimensional dynamic model with sharp interface formulation, J. Phys. D: Appl. Phys. 46 (5) (2013) 055501.
[62] Y. Yang, D. Gu, D. Dai, C. Ma, Laser energy absorption behavior of powder particles using ray tracing method during selective laser melting additive manufacturing of aluminum alloy, Mater. Des. 143 (2018) 12–19.
[63] Y. Bazilevs, V.M. Calo, J.A. Cottrel, T.J.R. Hughes, A. Reali, G. Scovazzi, Variational multiscale residual-based turbulence modeling for large eddy simulation of incompressible flows, Comput. Methods Appl. Mech. Engrg. 197 (2007) 173–201.
[64] A.N. Brooks, T.J.R. Hughes, Streamline upwind/petrov-galerkin formulations for convection dominated flows with particular emphasis on the incompressible navier–stokes equations, Comput. Methods Appl. Mech. Engrg. 32 (1982) 199–259.
[65] T.E. Tezduyar, Stabilized finite element formulations for incompressible flow computations, Adv. Appl. Mech. 28 (1992) 1–44.

[66] T.E. Tezduyar, Y. Osawa, Finite element stabilization parameters computed from element matrices and vectors, Comput. Methods Appl. Mech. Engrg. 190 (2000) 411–430.
[67] T.J.R. Hughes, L. Mazzei, A.A. Oberai, A. Wray, The multiscale formulation of large eddy simulation: Decay of homogeneous isotropic turbulence, Phys. Fluids 13 (2001) 505–512.
[68] T.J.R. Hughes, G. Scovazzi, L.P. Franca, Multiscale and stabilized methods, in: Encyclopedia of Computational Mechanics, John Wiley & Sons, 2004.
[69] M.C. Hsu, Y. Bazilevs, V.M. Calo, T.E. Tezduyar, T.J.R. Hughes, Improving stability of stabilized and multiscale formulations in flow simulations at small time steps, Comput. Methods Appl. Mech. Engrg. 199 (2010) 828–840.
[70] A. Masud, R. Calderer, A variational multiscale stabilized formulation for the incompressible navier–stokes equations, Comput. Mech. 44 (2) (2009) 145–160.
[71] L. Zhu, S. Goraya, A. Masud, Interface-capturing method for free-surface plunging and breaking waves, J. Eng. Mech. 145 (11) (2019) 04019088.
[72] R. Calderer, L. Zhu, R. Gibson, A. Masud, Residual-based turbulence models and arbitrary lagrangian–eulerian framework for free surface flows, Math. Models Methods Appl. Sci. 25 (12) (2015) 2287–2317.
[73] A. Masud, R. Calderer, Residual-based turbulence models for moving boundary flows: hierarchical application of variational multiscale method and three-level scale separation, Internat. J. Numer. Methods Fluids 73 (3) (2013) 284–305.
[74] L. Zhu, A. Masud, Variationally derived interface stabilization for discrete multiphase flows and relation with the ghost-penalty method, Comput. Methods Appl. Mech. Engrg. 373 (2021) 113404.
[75] A. Masud, M. Anguiano, I. Harari, Modeling of steep layers in singularly perturbed diffusion–reaction equation via flexible fine-scale basis, Comput. Methods Appl. Mech. Engrg. 372 (2020) 113343.
[76] J. Chung, G.M. Hulbert, A time integration algorithm for structural dynamics with improved numerical dissipation: the generalized-α method, J. Appl. Mech. 60 (2) (1993) 371–375.
[77] K.E. Jansen, C.H. Whiting, G.M. Hulbert, A generalized-α method for integrating the filtered navier–stokes equations with a stabilized finite element method, Comput. Methods Appl. Mech. Engrg. 190 (3–4) (2000) 305–319.
[78] N.M. Newmark, A method of computation for structural dynamics, J. Eng. Mech. Div. 85 (3) (1959) 67–94.
[79] J. Liu, W. Yang, M. Dong, A. Marsden, The nested block preconditioning technique for the incompressible navier–stokes equations with emphasis on hemodynamic simulations, Comput. Methods Appl. Mech. Engrg. 367 (2020) 113122.
[80] E. Olsson, G. Kreiss, S. Zahedi, A conservative level set method for two phase flow II, J. Comput. Phys. 225 (1) (2007) 785–807.
[81] A. Laadhari, P. Saramito, C. Misbah, Improving the mass conservation of the level set method in a finite element context, C. R. Math. 348 (9–10) (2010) 535–540.
[82] J. Yan, A. Korobenko, X. Deng, Y. Bazilevs, Computational free-surface fluid–structure interaction with application to floating offshore wind turbines, Comput. & Fluids 141 (2016) 155–174.
[83] M. Francois, S. Cummins, E. Dendy, D. Kothe, J. Sicilian, M. Williams, A balanced-force algorithm for continuous and sharp interfacial surface tension models within a volume tracking framework, J. Comput. Phys. 213 (1) (2006) 141–173.
[84] Z. Zhao, J. Yan, Variational multi-scale modeling of interfacial flows with a balanced-force surface tension model, Mech. Res. Commun. (2020) 103608.
[85] S. Lin, J. Yan, D. Kats, G. Wagner, A volume-conserving balanced-force level set method on unstructured meshes using a control volume finite element formulation, J. Comput. Phys. 380 (2019) 119–142.
[86] M. Herrmann, A balanced force refined level set grid method for two-phase flows on unstructured flow solver grids, J. Comput. Phys. 227 (4) (2008) 2674–2706.
[87] H. Montazeri, C. Ward, A balanced-force algorithm for two-phase flows, J. Comput. Phys. 257 (2014) 645–669.
[88] A. Klassen, T. Scharowsky, C. Körner, Evaporation model for beam based additive manufacturing using free surface lattice boltzmann methods, J. Phys. D: Appl. Phys. 47 (27) (2014) 275303.
[89] M. Bayat, A. Thanki, S. Mohanty, A. Witvrouw, S. Yang, J. Thorborg, N. Tiedje, J. Hattel, Keyhole-induced porosities in laser-based powder bed fusion (l-pbf) of ti6al4v: High-fidelity modelling and experimental validation, Addit. Manuf. 30 (2019) 100835.
[90] R. Cunningham, C. Zhao, N. Parab, C. Kantzos, J. Pauza, K. Fezzaa, T. Sun, A.D. Rollett, Keyhole threshold and morphology in laser melting revealed by ultrahigh-speed x-ray imaging, Science 363 (6429) (2019) 849–852.
[91] C. Zhao, N. Parab, X. Li, K. Fezzaa, W. Tan, A. Rollett, T. Sun, Critical instability at moving keyhole tip generates porosity in laser melting, Science 370 (6520) (2020) 1080–1086.